Dr. Eugene J. Maier 615

THEORY OF THE CIRCULAR PLANAR (GUARDRING) LANGMUIR PROBE

By

Lee W. Parker

Prepared under Contract No. NAS5-9088 by

MT. AUBURN RESEARCH ASSOCIATES, INC.
Cambridge, Massachusetts

For

Goddard Space Flight Center
NATIONAL AERONAUTICS AND SPACE ADMINISTRATION
Greenbelt, Maryland

12 April 1968

THEORY OF THE CIRCULAR PLANAR (GUARDRING) LANGMUIR PROBE

By

Lee W. Parker

Prepared under Contract No. NAS5-9088 by

MT. AUBURN RESEARCH ASSOCIATES, INC.
Cambridge, Massachusetts

For

Goddard Space Flight Center
NATIONAL AERONAUTICS AND SPACE ADMINISTRATION
Greenbelt, Maryland

12 April 1968

ABSTRACT

A computational study is presented of the properties of a guardring-type circular planar Langmuir probe, commonly flush-mounted in the skin of a satellite. This geometry results in a three-dimensional potential distribution which cannot be treated analytically, even in axially symmetric problems. Given arbitrary particle velocity distributions at infinity, the current-voltage characteristics of the external aperture grid and of an internal repelling collector (for attractive aperture grid potentials) may be determined by detailed particle trajectory calculations. The electric field and charge density distributions in the vicinity of the probe are defined at the nodes of a grid. The charge density in the Poisson equation is evaluated by summing trajectory contributions. The collected currents are similarly evaluated. The Poisson field is computed self-consistently by an iterative technique. Two kinds of particle velocity distribution are considered, e.g., a streaming Maxwellian at infinity, and photoelectric (or secondary) emission at the satellite surface. An infinite-satellite model is assumed for the Poisson case (Debye length = 1 cm). For the Laplace case (Debye length infinite), the effects of finite satellite dimensions, of Mach streaming at an angle, and of photoelectrons are investigated.

TABLE OF CONTENTS

TABLE OF CONTENTS (continued)

I. INTRODUCTION

The work of this report is concerned with computer methods for calculating the particle velocity distribution at (and the current collected by) a circular planar probe in a collisionless plasma.(1-2) This probe, illustrated in Fig. 1, is commonly flush-mounted on satellites,(3) and is geometrically similar to a laboratory planar guard-ring probe.(4) There is no exact analytic theory available for this multi-dimensional probe. However, an approximate theory for the central point is given in Ref. 2, based on velocity space analysis. The theory of Ref. 2 will be considered as supplementary to this report and will not be repeated here. Rather, the computational aspects of the problem, which are treated only briefly in Ref. 2, will be given primary attention. The determination of the electric field configuration, in other words, the structure of the sheath, is the heart of the problem.

The present computer program is capable of evaluating either the particle number density or the current density, i.e., moments of the velocity distribution, at an arbitrary point in space. Either moment may be expressed as an integral of the phase space density over velocity space. Replacement of the (triple) integral by an approximating Gaussian quadrature sum is equivalent to consideration of a finite number of trajectories (to represent all possible trajectories passing through the point). On each trajectory, the phase space density is constant. The trajectories are dynamically reversible in the time-independent field, and by following each trajectory backwards in time to its origin, where the phase space density is considered known, one may evaluate the terms in the quadrature sum. The word "origin" means infinity or an emitting surface.

The electrostatic potential configuration is represented by a grid, at the points of which the potential is defined. The electric field is defined by interpolation. The boundary of the grid represents the surface at "infinity" for computational purposes. Thus, the net charge density can be evaluated at each grid point by calculating separately the contributions of attracted and repelled particles, in any fixed potential distribution.

However, the potential distribution is not known and depends in turn on the charge density, as well as the probe and satellite potentials, through the Poisson equation. Thus, the charge density and potential distributions must be made self-consistent.

An iteration technique seems to be the only feasible means for accomplishing this task. Progress has been made along these lines for the special (one-dimensional) cases of spherical and cylindrical probes in a plasma at rest.(5) When the Laplacian operator is approximated by a difference operator on the grid, there results a set of non-linear equations for the values of the potential (alternatively, the density) at the grid points. The iteration technique is applied to this set of equations. Whether the iteration converges or not depends on the boundary condition, in the following way.

The condition that the potential must fall off to zero at infinity requires special treatment when we employ a grid of finite dimensions. In the present investigation, for each case a sequence of problems is solved, in which the only parameter which changes is the outer grid dimension, or effective grid boundary radius. The value of the collected current depends strongly on the grid radius when this radius is small. As the radius is increased, however, the current tends toward a "stationary" value. It is this stationary value which corresponds to the infinite boundary condition. This behavior has also been noted in Ref. 5.

Unfortunately, obtaining the solution is not only a matter of moving the grid boundary outward in steps and re-solving the problem at each step, while monitoring the collected current, until the desired degree of "stationariness" is attained. As the boundary is moved outward, the iteration process itself tends to become unstable and diverge. Therefore, a sophisticated iteration scheme has been developed in which successive density (or potential) iterates are linearly combined, or "mixed". (This method is also used in Ref. 5.) The iteration can, in this way, be made to converge for any boundary radius by suitably adjusting the mixing ratio. However, the number of iterations required, and therefore the computing time, would grow with increasing boundary radius.

There are other numerical parameters which must be considered such as grid mesh size, trajectory step size (accuracy), and number of trajectories per space point. The computed current must be "stationary" with respect to changes in these parameters, as well. Among these parameters, trajectory step size has been found to be most critical, and grid mesh size least critical.

Calculations have been performed for two types of particle velocity distribution, namely, a streaming Maxwellian at infinity (Secs. II - VII), and photoelectric (or secondary) emission at the satellite surface (Sec. VIII).

In Sec. II, the forms of the moment integrals (particle and current density) are considered,with contributions in velocity space separated into two parts, namely, contributions from infinity, and contributions from nearby surfaces.

In Sec. III, the moment integrals are specialized to energy-angle velocity space.

In Sec. IV, the satellite is assumed to be an infinite plane, and calculations are discussed for the Laplace field (infinite Debye length). The current-voltage characteristic of the circular planar probe is linear at large probe potentials. This linearity is consistent with experimental data obtained in guard-ring probe measurements.(4)

In Sec. V, solutions of the sheath problem (Poisson field) and attracted-particle currents are discussed. The Debye length is equal to

0.3 probe radii, the probe potential energy is -45.54 kT, and the satellite is infinite. The current density at the central point, for Mach zero, is 33.3, in units of the current at zero potential. This value is nearly the same as the corresponding value for the Laplace field, namely, 35.5, thus indicating approximate independence of the central current density with respect to Debye length. This result is predicted by the theory of Ref. 2. The current density on the probe surface falls off more rapidly with radius in the Poisson field than in the Laplace field. Thus, the current collected by a finite area, relative to the current at zero potential, would be less at small Debye lengths than at large Debye lengths (for equal probe potentials). This accounts for the Poisson value of 25 versus the Laplace value of 36, when the collecting radius is an appreciable fraction, i.e., 1/2, of the probe radius.(1) Some computational aspects of the Poisson problem are also discussed in Sec. V. Tests with different boundary laws (floating-dipole and zero-potential) show the stationary value of the current to be independent of these laws. Moreover, tests made with increasing grid boundary radii show that the current approaches its stationary value rapidly for grid radii greater than about 1.5 probe radii.

In Sec. VI, the velocity distribution at the aperture grid is considered, especially the distribution in normal components of velocity. The latter distribution determines the current collected by an internal collector which is biased relative to the aperture grid, which has a fixed attractive potential. When the collector is repulsive with respect to the plasma, its current characteristic approximates that of a simple repelling probe, regardless of the fact that the aperture grid is attractive. The approximation becomes improved when the collecting area is restricted to a small region at the center of the probe. The theory of Ref. 2 provides an explanation for this behavior. When the collector is attractive with respect to the plasma, the current rises linearly for some range of the collector potential, and subsequently levels off.(2)

Section VII deals with the isolated satellite in the form of a truncated cylinder. The calculations yield the same central-point current density, in the Laplace field, as that obtained for the infinite satellite. This agreement is due to the large dimensions of the satellite (of the order of a meter) compared with the probe radius (a few cm). The Poisson field was not calculated, but at small Debye lengths the current should be even less dependent on the satellite size than in the Laplace field. When the particle velocity distribution is a Maxwellian with Mach number M and Mach vector angle γ with respect to the probe normal, the current divided by $M\cos\gamma$, which would be constant in one-dimensional infinite-plane geometry, falls off instead with increasing γ.

In Sec. VIII, test calculations are discussed for monoenergetic photoelectrons emitted at the surface of the isolated satellite and collected in the Laplace field of the probe. The intensity of emission at a point is proportional to the cosine of the angle of incidence of solar radiation. The collected current is found to be a maximum when the solar radiation is incident along the axis of the probe (solar angle zero), and to fall off as the solar angle increases.

In Appendix A, the difference equations for the Laplace or Poisson problems are derived for the infinite and isolated satellites, and the method of solution is given for the linear equations.

In Appendix B, the conversion of moment integrals to Gaussian quadrature (trajectory) sums is treated.

In Appendix C, the equations of motion and the method of interpolation in the grid are discussed for the trajectory calculations. A step-size control for trajectory accuracy is also given.

In Appendix D, the iteration process is discussed.

In Appendix E, the problem with fixed zero potential on the boundary is considered in detail. All steps of the iteration process are presented in order to illustrate the method of computation.

In Appendix F, test calculations are discussed which illustrate how changes at the grid boundary affect computed values of current and density.

II. INTEGRALS AND DOMAINS IN VELOCITY SPACE

The considerations of this section are based on the assumption of a fixed field configuration. The scalar particle density $n(\vec{r})$ and the vector current density $\vec{j}(\vec{r})$ at a point $\vec{r}$ in ordinary space may be written as triple integrals over velocity space of the form

$$n(\vec{r}) = \iiint f(\vec{r}, \vec{v})\, d^3\vec{v} \tag{2-1}$$

$$\vec{j}(\vec{r}) = \iiint \vec{v}\, f(\vec{r}, \vec{v})\, d^3\vec{v} \tag{2-2}$$

where $\vec{v}$ is the vector velocity of a particle passing through the point $\vec{r}$. The distribution function $f(\vec{r}, \vec{v})$ is the density of points in six-dimensional phase space. In the time-independent collision-free case, and where the particles move under conservative forces, the energy E is constant along any trajectory. The function f in (2-1) and (2-2) depends only on the constants of motion and thus is constant along each trajectory. That is, each trajectory, characterized by a pair of vectors $(\vec{r}, \vec{v})$, connects points of equal values of f.

The region of interest may be considered to be enclosed by a composite boundary surface where the phase density is assumed known. The boundary consists of two portions. One portion is the "external" surface at infinity, where an unperturbed particle velocity distribution is assumed to exist, e.g., a streaming Maxwellian in the form:

$$f_\infty\ (v_\infty, \alpha_\infty) = n_o \left(\frac{m}{2\pi kT}\right)^{3/2} e^{-u^2} \tag{2-3}$$

where

$$u^2 = \frac{m}{2kT} (v_\infty{}^2 + v_o{}^2 - 2v_\infty v_o \cos\theta_\infty) \tag{2-4}$$

In (2-3), n_o is the unperturbed particle density, m is the particle mass, T is the temperature, $\vec{v}_\infty$ is the velocity at infinity, $\vec{v}_o$ is the streaming (Mach) velocity, and θ_∞ is the angle between $\vec{v}_\infty$ and $\vec{v}_o$. The distribution (2-3) replaces the function f whenever $\vec{r}$ and $\vec{v}$ define a trajectory which connects with infinity.

The other portion of the boundary consists of "internal" surfaces in the near vicinity, such as the probe and satellite surfaces. If these internal surfaces emit particles such as photoelectrons or secondary electrons, then there is a non-vanishing distribution f_s which appears in (2-1) and (2-2) whenever $\vec{r}$ and $\vec{v}$ define a trajectory which connects with the surface.

Disregarding trajectories corresponding to trapped particles, we see that (2-1) and (2-2) may be resolved into the sum of two triple integrals, namely,

$$n(\vec{r}) = n_\infty + n_s = \iiint_\infty f_\infty \, d^3\vec{v} + \iiint_s f_s \, d^3\vec{v} \tag{2-5}$$

$$\vec{j}(\vec{r}) = \vec{j}_\infty + \vec{j}_s = \iiint_\infty \vec{v} f_\infty \, d^3\vec{v} + \iiint_s \vec{v} f_s \, d^3\vec{v} \tag{2-6}$$

where the first integral in each equation is comprised of all contributions coming from infinity, and the second integral is comprised of all contributions coming from the near surfaces.

The whole of local velocity space, i.e., the vector space $\vec{v}$, is therefore divided in two domains, one corresponding to connections with infinity, and the other corresponding to connections with a near surface. There is a surface of demarcation separating these two domains in velocity space. This surface may be traced out by trajectory calculations.

In order to determine whether a specified velocity $\vec{v}$ (at $\vec{r}$) connects with infinity or with a near surface, the trajectory may be followed backwards in time to its origin (all trajectories being dynamically reversible). In general, this is a task for a computer, and a computational scheme is outlined in the next section.

III. DENSITY AND CURRENT

Since isotropic velocity distributions are frequently of interest, it will be convenient to express the velocity space volume elements of Sec. II in polar form. Thus, (2-1) and (2-2) become

$$n\,(\vec{r}) = \iiint\limits_{\text{sphere}} f\,v^2\,dv\,d\Omega \tag{3-1}$$

$$j\,(\vec{r}) = \iiint\limits_{\text{hemisphere}} f\,v^3\,dv\,\cos\alpha\,d\Omega \tag{3-2}$$

where we have expressed the volume element by

$$d^3\,\vec{v} = v^2\,dv\,d\Omega, \quad d\Omega = \sin\alpha\,d\alpha\,d\beta \tag{3-3}$$

and where v, α, and β are the magnitude, polar angle, and azimuthal angle, respectively, of the velocity vector $\vec{v}$. The scalar equation (3-2) implies that j is the component of the current density vector $\vec{j}$ in the direction of the chosen axis (e.g., the normal to the probe surface). In (3-1) the angular integration is over the sphere (4π steradians), while in (3-2) the angular integration is over the forward hemisphere (2π steradians).

More useful forms for the equations are obtained if the integration over v is converted into an integration over kinetic energy E of the particles at the emitting surface. Thus, when the potential energy is a function $\Phi(\vec{r})$ with respect to the emitting surface, we have the differentials:

$$v^2\ dv = \left(\frac{2}{m^3}\right)^{1/2} (E-\phi)^{1/2}\ dE \qquad (3\text{-}4)$$

and

$$v^3\ dv = \frac{2}{m^2} (E-\Phi)\ dE \qquad (3\text{-}5)$$

where $E-\phi$ is required to be positive. Otherwise, the differentials vanish. Note that the total energy for the trajectory is $E+\Phi_s$, where Φ_s is the potential energy of the emitting surface.

For concreteness, assume that there is a streaming Maxwellian velocity distribution at infinity with streaming velocity v_o, and an isotropic emission (e.g., secondary or photoelectric) function at the satellite surface outside the probe. Then the density integrals are given by the following formulae:

$$n = n_\infty + n_s \qquad (3\text{-}6)$$

where (see Sec. II)

$$n = \frac{n_o}{2\pi^{3/2}} \int_{\mathrm{Max}(\phi,0)}^{\infty} dE\ (E-\phi)^{1/2} \iint_{\infty\ (\mathrm{sphere})} e^{-u^2}\ d\Omega \qquad (3\text{-}7)$$

with (see Equation (2-4))

$$u^2 = E + M^2 - 2E^{1/2} \cos\theta_\infty \qquad (3\text{-}8)$$

$$E \equiv mv_\infty^2/2kT, \qquad M^2 \equiv mv_o^2/2kT, \qquad \phi \equiv \Phi/kT \tag{3-9}$$

and

$$n_s = \iint\limits_{s\ \text{(sphere)}} \frac{d\Omega}{4\pi}\, n_{so}(\vec{r}_s) \int_{\text{Max}(\Phi,0)}^{\infty} \frac{f_s(E, \vec{r}_s)\, dE\, (E-\Phi)^{1/2}}{\left[\int_0^\infty f_s\, (E, \vec{r}_s)\, E^{1/2}\, dE\right]} \tag{3-10}$$

The symbol Max(p, 0) is defined to be p if $p > 0$, and zero if $p < 0$. In (3-7), E, ϕ, and M are the dimensionless energy, potential, and Mach number according to (3-9), and Φ is the local potential relative to infinity, where the density is n_o. Moreover, the integral over solid angles in (3-7) includes only directions such that the trajectories of dimensionless energy E originate at infinity. In (3-10), E is dimensional, $f_s(E, \vec{r}_s)$ is the kinetic energy distribution of emitted particles at the trajectory emission point $\vec{r}_s$, n_{so} is the density of emitted particles at the point $\vec{r}_s$, and the integral over solid angles includes only directions such that the trajectories of kinetic energy E originate at the satellite surface. Note that $\vec{r}_s$ depends on the trajectory, and that Φ is the local potential energy relative to the satellite.

Similarly, the probe current integrals at a point $\vec{r}$ on the probe surface are given by the following formulae:

$$j = j_\infty + j_s \tag{3-11}$$

where

$$j_\infty = n_o \left(\frac{kT}{2\pi m}\right)^{1/2} \int_{\text{Max}(\phi,0)}^{\infty} dE\, (E-\phi) \iint\limits_{\infty\ \text{(hemisphere)}} e^{-u^2}\, \frac{\cos\alpha\, d\Omega}{\pi} \tag{3-12}$$

with u^2 defined by (3-8) and (3-9), and

$$j_s = \iint\limits_{s\ \text{(hemisphere)}} \frac{\cos\alpha\ d\Omega}{\pi}\, j_{so}(\vec{r}_s) \int_{\text{Max}(\Phi,0)}^{\infty} \frac{f_s\ (E,\ \vec{r}_s)\ dE}{\left[\int_0^{\infty} f_s\ (E,\ \vec{r}_s) dE\right]} \left(\frac{E-\Phi}{\overline{E}}\right) \qquad (3\text{-}13)$$

The quantities in (3-12) are defined as in (3-7), and the quantities in (3-13) are defined as in (3-10), with $\vec{r}_s$ being the point of origin of the trajectory on the satellite surface. Here, j_{so} is the normal component of current density of emitted particles at the point $\vec{r}_s$, and $\overline{E}$ is the mean kinetic energy of the emitted particles. Note that (3-13) assumes isotropic emission at the point $\vec{r}_s$. This is equivalent to assuming a "cosine law" for the current density per unit solid angle.

Equation (3-11) is based on the assumption of no emission from the probe surface. If such emission were to be considered, an integral of the form of (3-13), but counting only trajectories which originate at other points $\vec{r}_s$ on the probe surface, would give that part of the current density which returns to the probe at the point $\vec{r}$.

IV. PROBE CURRENT IN LAPLACE FIELD -- INFINITE SATELLITE

If the satellite in whose skin the circular planar probe is mounted is so large that its dimensions are large compared with an effective length characterizing the range of the potential field of the probe, then the satellite may be represented to a good approximation by an infinite flat plane. This approximation is consistent provided the satellite is at the plasma potential. The geometry may then be well represented by an infinite plane held at zero potential, as in Fig. 2, in which there is a circular region (i.e., the probe) held at potential (energy) $\Phi_o = -V_o$. Figure 2 idealizes the OGO probe, which consists of an outer grid and an inner collector (plus intermediate grids not shown).

Letting r and z denote cylindrical radial and axial coordinates, respectively, the potential distribution is given, for infinite Debye length, by the Laplace solution:

$$\Phi(r, z) = \Phi_o \int_o^\infty e^{-z} J_1(x) J_o (xr) dx \qquad (4\text{-}1)$$

where r and z are multiples of the probe radius. A large tabulation and contours of the integral in (4-1) are given in Ref. 1. (See also Table 1.) In the fixed potential field defined by (4-1) or Table 1, the current density of attracted particles coming from a streaming Maxwellian velocity distribution at infinity is computed by evaluating Equation (3-12) numerically.

In order to do this, we replace (3-12) by a quadrature sum, as shown in Appendix B, in the form:

$$\frac{j}{j_o} = \int_{-1}^{1} \frac{2dx}{(1-x)^2}\left[\frac{1+x}{1-x} + E_{min} - \phi\right]\int_{-1}^{1}\frac{dy}{2}\int_{-1}^{1}\frac{dz}{2}\,\delta e^{-u^2} \qquad (4-2)$$

$$\cong \frac{1}{2}\sum_k\sum_\ell\sum_m H_k\, H_\ell\, H_m \frac{\left[\frac{1+x_k}{1-x_k} + E_{min} - \phi\right]}{(1-x_k)^2}\,\delta_{k\ell m} e^{-u^2_{k\ell m}} \qquad (4-3)$$

where j is evaluated at a radial position $\vec{r}_p$ on the probe, $j_o = n_o(kT/2\pi m)^{1/2}$ is the random current density at infinity, δ is a Heaviside function which is unity if the trajectory connects with infinity, and $E_{min} = \text{Max}\ (\phi,0)$ is the lower limit of the energy integral. In obtaining (4-2) we have made the transformations

$$E = (1 + x)/(1 - x) + E_{min} \qquad (4-4)$$

$$\sin^2\alpha = (y + 1)/2 \qquad (4-5)$$

$$\beta = \pi(z + 1) \qquad (4-6)$$

where x, y, and z vary in the range (-1, 1). Then Gaussian quadrature formulae may be employed for each of these variables, with abscissae x_k, y_ℓ, and z_m, so that $E_k = E(x_k)$, $\alpha_\ell = \alpha(y_\ell)$, and $\beta_m = \beta(z_m)$ through (4-4) - (4-6). The associated coefficients are H_k, H_ℓ, and H_m, respectively. The index triplet (k, ℓ, m) in the sum (4-3) defines a single trajectory at the point $\vec{r}_p$, which may be traced backwards in time according to the prescription in Appendix C. The quantity $u^2_{k\ell m}$ in the exponential of (4-3) is the value of u^2 given by (3-8) at the end of the trajectory, and the quantity $\delta_{k\ell m}$ is defined to be unity if the trajectory is found to come from infinity, and zero otherwise. The number of triplets, or terms in the sum (4-3), is equal to the total number of trajectories. If the streaming direction is parallel to the probe axis, there is no preferred azimuthal plane; then symmetry allows us to replace π by $\pi/2$ in (4-6) and thus obtain higher quadrature accuracy in the β-integration, with the same Gaussian order. If the field is axially symmetric (e.g., the Laplace field), the β-integration is trivial at the central point of the probe.

The current-collecting area (aperture) was defined to have a radius R = 1.665 cm, i.e., one-half of the probe radius 3.33 cm, in these calculations. If r and θ denote the radial and azimuthal coordinates of a point, the current collected by the aperture is given by an integration over the surface area, namely:

$$\frac{I}{I_o} = \int_o^{2\pi} \frac{d\theta}{2\pi} \int_o^R \left(\frac{j}{j_o}\right) \frac{dr^2}{R^2} = \int_{-1}^{1} \frac{da}{2} \int_{-1}^{1} \left(\frac{j}{j_o}\right) \frac{db}{2} \tag{4-7}$$

$$\cong \frac{1}{4} \sum_p \sum_q H_p H_q \left(\frac{j}{j_o}\right)_{pq} \tag{4-8}$$

where the transformations have been made:

$$\theta_p = \pi(a_p + 1) \tag{4-9}$$

$$r_q = R[(b_q + 1)/2]^{1/2} \qquad (4\text{-}10)$$

In (4-7) and (4-8), $I_o = \pi R^2 j_o$, and in (4-9) and (4-10), a_p and b_q are the Gaussian abscissae for the azimuthal angle and radial integrations, respectively. If the streaming direction is parallel to the probe axis, the azimuthal integral is trivial since j is independent of θ.

In all calculations for the infinite satellite case, the streaming direction was parallel to the probe axis. For the Laplace field, the currents were found to be essentially independent of the grid boundary position beyond about two probe radii.

Table 2 gives computed current of ions collected by the aperture (in multiples of the current at zero potential), at Mach zero, as a function of aperture potential energy (in multiples of kT). The potential energy is negative in the ion-attraction range. In the left-hand column, the voltage equivalent is given for an assumed temperature of 1300°K. In order to calculate these currents (see Appendices A and B), the Laplace potential given by (4-1) was represented on a grid with outer boundaries at r = z = 3a, where a is the probe radius (3.33 cm). The grid was divided into 12 equal intervals in both r and z. (Figure A-1 shows such a grid with 6 intervals in r and z.) Thus, $\Delta r = \Delta z = a/4$ (or 0.8325 cm) for 12 intervals, and a/2 for 6 intervals. The currents were calculated using 16 values of k, 8 values of ℓ, and 8 values of m in (4-3), and 3 values of q in (4-8), that is, a fairly coarse resolution. The trajectory step length was selected to be 0.24 Δr (or 0.2 cm). Subsequent work shows that the value of the current depends strongly on the step size or trajectory accuracy (see Appendix C); for the rather coarse step size used (0.2 cm), the currents in Table 2 are estimated to have errors of the order of 5% at the highest potentials, and less in the low-potential range. The most striking result is the linear behavior of the current, with slope very close to 3/4. A theoretical justification of this linear behavior and slope is given in Ref. 2. Also, the behavior of an experimental circular planar guard-ring probe in the laboratory is consistent with these calculations.(4)

Table 3 gives the computer current at various Mach numbers in the Laplace field, with probe potential fixed at -45.54 kT, corresponding to -5.1 volts at 1300°K. The current is given in multiples of the zero-potential current, so that this ratio approaches unity at large Mach numbers. The grid employed had outer boundaries at $r = 3a$ and $z = 1.5a$, with 6 equal intervals in each direction. The step size was .025 cm, or $0.03\ \Delta z = 0.015\ \Delta r$. The current densities at 3 radial positions are also given in Table 3. The variation with radius of these current densities should diminish with increasing Mach numbers. The fact that the radial variation is not reduced with increasing Mach numbers indicates that the number of trajectories employed (i.e., the orders of the Gaussian quadratures) must be increased to maintain accuracy at large Mach numbers.

Table 3 replaces the curve in Fig. 5 of Ref. 1, which is somewhat in error since it was computed with a very large step size (0.8 cm).

V. PROBE CURRENT IN POISSON FIELD -- INFINITE SATELLITE

For the Poisson problem, the grid (Appendix A) employed for defining the potential field may also be used for defining the particle density distributions. The numerical problem to be solved may be expressed in a schematic vector form in terms of dimensionless quantities, namely:

$$L\vec{\phi} = \vec{n}_e(\vec{\phi}) - \vec{n}_i(\vec{\phi}) \tag{5-1}$$

Equation (5-1) represents the Poisson equation in difference form (Appendix A) as a set of N simultaneous equations with N unknowns, where N represents the number of grid points where the potentials and densities are to be evaluated. The values of the potential at the grid points are considered to be components of an N-dimensional vector $\vec{\phi}$, and the values of the electron and ion particle densities at the grid points are also components of N-dimensional vectors $\vec{n}_e$ and $\vec{n}_i$, respectively. The operator L in (5-1) is the matrix operator derived from the differencing of the Laplacian operator. The right-hand side of (5-1) expresses the fact that each component of $\vec{n}_e$ or $\vec{n}_i$ generally depends on more than one component of $\vec{\phi}$.

Since the relationship between $\vec{n}_e$, $\vec{n}_i$ and $\vec{\phi}$ is non-linear, an iteration procedure must be used. Starting with a (zero-order) guess for $\vec{\phi}$, for example, the Laplace field, we calculate first-order vectors $\vec{n}_e$ and $\vec{n}_i$ in this field (Appendix B), and solve (5-1) for a new (first-order) $\vec{\phi}$. Iteration continues until the right-hand and left-hand sides of (5-1) are consistent. If one actually starts with the Laplace solution, i.e., if the initial guess is poor, the procedure may diverge unless a suitable artificial damping process is imposed. Appendix D treats the problem of iteration with damping, which is introduced through the coupling or mixing of successive iterates. In general, the tendency of the iteration to diverge depends on the position of the boundary. If the boundary is very near (to the probe), the iteration is stable even without damping. But since the desired current must correspond to a theoretical boundary at infinity, the computational boundary must in practice be placed at a sufficiently great distance that its position does not affect the current. At the same time, however, the direct iteration without damping becomes highly unstable, and the solution is difficult to achieve. Experience indicates that with sufficiently strong damping one may always obtain a solution, at the cost of increasingly lengthy computing time.

The calculations presented in Appendix E illustrate the method of iteration with mixing.

Self-consistent Poisson solutions at Mach zero (Table 4) and Mach 3 (Table 5) have been obtained for a Debye length of 1 cm, i.e., 3/10 of the probe radius (3.33 cm), at a probe potential of -45.54 kT (-5.1 volts with T = 1300°K).

For the Mach zero case, the total current collected in the Poisson field with Debye length 1 cm, by an area 1.665 cm in radius, is 25 (Table 6) in multiples of the zero-potential current. For the same problem but with infinite Debye length, i.e., the Laplace field, the total current is 36 (Table 6). These values for the total current (of either attracted ions or attracted electrons) were obtained by integrating the current density over the circular collecting area, using 3 radial points. (See (4-8).) Table 6 gives the values of the total collected current and of the current density at the 3 radial points, in multiples of the zero-potential values. Also given is the current density at the central point, namely 35.5 and 33.3 for the Laplace and Poisson fields, respectively. These current densities are the most accurate available values, having been computed with 64 values of k and ℓ.

The central-point current density was calculated using fine trajectory resolution, namely, 64 values of k and 32 values of ℓ in

(4-3), and small step size, to obtain high accuracy. It is interesting that the current density is nearly the same for the Poisson and Laplace fields, i.e., 33.3 and 35.5, respectively. The central current density has been treated theoretically for the Mach zero case in Ref. 2. There it is shown, on the basis of an impulse approximation employing straight-line trajectories, that the central current density is approximately independent of Debye length (i.e., of the shape of the potential fall-off). However, Table 6 shows that the current density falls off with increasing radius more rapidly in the Poisson case than in the Laplace case (in which it is nearly constant). This accounts for the fact that the current collected by a finite area in the Poisson case is considerably less than in the Laplace case. It may be expected that as the Debye length gets small, the current density will drop off more and more rapidly with radius.

For the Mach 3 case, the total collected ion current is 2.4 for the Poisson field, and 3.2 for the Laplace field. There is no noticeable fall-off in current density with radius. However, the values are not accurate since too few trajectories were used.

The grid employed for the Poisson density and potential calculations was the same as that used for the Laplace field current calculations (Appendix A). The difference equations were tested by comparing their solution in the Laplace case with the exact solution (e.g., Table 1). A solution of adequate accuracy (in the sense of small variations in the current) was obtained using a grid with outer boundaries at r and z in excess of about 2 and 1.5 probe radii, respectively. The role played by the fineness of the grid mesh, i.e., the size of the grid intervals Δr and Δz, is not yet well established. Currents calculated with 6-interval or 12-interval grids seem considerably less sensitive to trajectory accuracy than 3-interval grids. Similar observations apply to density calculations.

Test calculations were made with a series of Poisson problems with increasing values of z at the boundary, to determine the boundary position beyond which the current becomes stationary. These tests indicate that boundary values of z greater than 1.5 probe radii are probably adequate, and that one should certainly be safe at 3 probe radii.

A dipole law was assumed at the grid boundary in order to allow the potential to float. (The dipole law is the correct asymptotic law for the Laplace field.) This procedure has been found in spherically symmetric probe calculations(5) to be more efficient than that of fixing the potential to be zero. In the present work, a zero-potential boundary problem (Appendix E) was solved, yielding the same central current density (within 3%) as the dipole boundary problem.

Selected numerical results bearing on some of the above questions are discussed in Appendix F.

The ion and electron particle densities are tabulated, for the Poisson Mach zero problem in Tables 7 and 8, and for the Poisson Mach 3 problem in Tables 9 and 10. The trajectory step-sizes used at the various grid points are indicated by the numbers in parentheses in the ion density tables. These were determined by tests, at each point, on the approach of the densities toward stationary values. (See Appendix E for illustration.) The difference scheme used for these calculations (Appendix A) did not require the values of the densities either at points on the boundary or on the axis.

The density calculation is performed by replacing (3-7) by a transformed integral and quadrature similar to (4-2) and (4-3), namely:

$$\frac{n}{n_o} = \frac{1}{\sqrt{\pi}} \int_{-1}^{1} \frac{2dx}{(1-x)^2} \left[\frac{1+x}{1-x} + E_{min} - \phi\right]^{1/2} \int_{-1}^{1} dy \int_{-1}^{1} \frac{dz}{2}\, \delta e^{-u^2} \qquad (5\text{-}2)$$

$$\cong \frac{1}{\sqrt{\pi}} \sum_{k} \sum_{\ell} \sum_{m} H_k \, H_\ell \, H_m \, \frac{\left[\frac{1 + x_k}{1 - x_k} + E_{min} - \phi\right]^{1/2}}{(1 - x_k)^2} \, \delta_{k\ell m} \, e^{-u^2_{k\ell m}} \qquad (5\text{-}3)$$

where (5-3) is similar in form to (4-3), with similarly defined quantities. However, although the energy and azimuthal angle transformations are identical to (4-4) and (4-6), the polar angle transformation is given by $\cos\alpha = y$ instead of (4-5). (See Appendix B.)

For the density calculations, 16 values of k, 8 values of ℓ, and 8 values of m were used at each density point. These numbers were determined on the basis of tests with the Laplace field, which is relatively slowly-varying. The same number of trajectories, i.e., 1024, was used at each point for the Poisson problems as well, although the more rapid variation of potential probably requires higher trajectory resolution (more trajectories) to maintain low error at individual density points. This coarse resolution was employed in the interest of saving computer time, with the expectation that for the final current the net error would probably be less than that of any individual density. The required resolution should be increased with increasing Mach number, however, and therefore the Poisson results in the Mach 3 case must be considered as much more approximate than those in the Mach zero case.

VI. VELOCITY DISTRIBUTION AT THE APERTURE. RETARDED CURRENT.

Let the aperture grid of the probe be at a fixed attractive voltage with respect to the plasma, and let a parallel collector behind the aperture grid have a variable bias relative to the aperture grid, as illustrated in Fig. 2. If the collector is attractive with respect to the aperture grid, then all of the current passing through the aperture is collected by the collector. The current-collection formulae discussed in the previous sections refer, therefore, to the current collected by a collector which is at zero (or attractive) potential relative to the aperture grid. If the collector is repulsive with respect to the aperture grid, the current is reduced, and the shape of the curve of collected current versus repulsive collector potential depends on the distribution of normal components of velocity at the aperture surface. In the experimental situation of the circular planar probe geometry, it is particularly convenient to place a repulsive collector (with various screening grids) behind the aperture grid, and thereby analyze the current for information regarding the velocity distribution at infinity.

The theoretically expected current to the collector may be computed by trajectory summations similar to (4-3) and (4-8). It is more convenient for this problem to use cylindrical polar or cartesian coordinates than spherical polar coordinates. Thus, letting the normal direction define the z-axis of the coordinate system, we may obtain a distribution in z-components of velocity v_z by integrating over the v_p and β (or v_x and v_y) coordinates, where v_p is the projection of $\vec{v}$ on the x-y plane, i.e., the "perpendicular" component of velocity defined by $v_p^2 = v_x^2 + v_y^2$, and β is the azimuthal angle of the plane containing $\vec{v}$. Thus, the volume element in (2-2) becomes

$$d^3 \vec{v} = v_p \, dv_p \, d\beta \, dv_z \qquad (6\text{-}1)$$

and, assuming a streaming Maxwellian velocity distribution at infinity as defined by (2-3), the current density integral of (3-12) may be expressed as(assuming $\phi < 0$):

$$\frac{j}{j_o} = \int_o^{-\phi} dZ \int_o^{2\pi} \frac{d\beta}{2\pi} \int_{-\phi-Z>0}^{\infty} dX \; \delta e^{-u^2} + \int_{-\phi}^{\infty} dZ \int_o^{2\pi} \frac{d\beta}{2\pi} \int_o^{\infty} dX \; \delta e^{-u^2} \qquad (6\text{-}2)$$

where

$$X \equiv m \, v_p^{\;2}/2kT, \qquad Z \equiv m \, v_z^{\;2}/2kT, \qquad j_o \equiv n_o(kT/2\pi m)^{1/2} \qquad (6\text{-}3)$$

$$u^2 = E + M^2 - 2E^{1/2} M \cos\theta_\infty \qquad \text{Sec. III(3-8)}$$

$$E = X + Z + \phi \qquad (6\text{-}5)$$

and M and ϕ are defined in (3-9). The function δ is a Heaviside function, as in (4-2). The lower limit on the X-integration in (6-2) is, in each range of Z, such as to correspond to vanishing total energy at infinity. From the form of (6-2), we see that the distribution in kinetic energies Z associated with the z-components of velocity at the aperture grid is defined by

$$\frac{d}{dZ}\left(\frac{j}{j_o}\right) = \int_o^{2\pi} \frac{d\beta}{2\pi} \int_{\mathrm{Max}(0,\ -\phi\ -Z)}^{\infty} dX\ \delta e^{-u^2} \tag{6-6}$$

The distribution function (6-6), which will be simply referred to here as "dj/dZ", is discussed in Ref. 2 for the central point (i.e., the β-integration gives unity). For the Mach zero case, if we assume $\delta = 1$ for all X (no "intersections" in the sense of Ref. 2), then

$$\frac{d}{dZ}\left(\frac{j}{j_o}\right) = 1 \qquad \text{for} \quad Z < -\phi \tag{6-7}$$

$$= e^{-Z\ -\phi} \quad \text{for} \quad Z > -\phi \tag{6-8}$$

Equation (6-8) suggests a Druyvesteyn relation$^{(2)}$. If the collector is at a repulsive potential Δ with respect to the aperture, the collected current density at a point is the integral of (6-6) from $Z = \Delta$ to $Z = \infty$. Thus, if $\delta = 1$, (6-7) and (6-8) yield the "retarded" collector current ($\Delta \geq 0$):

$$\frac{j'}{j_o} = \int_{\Delta}^{\infty} \frac{d}{dZ}\left(\frac{j}{j_o}\right) dZ$$

$$= 1 - (\Delta + \phi) \qquad \text{if} \quad \Delta + \phi < 0 \tag{6-9}$$

$$= e^{-(\Delta + \phi)} \qquad \text{if} \quad \Delta + \phi > 0 \tag{6-10}$$

Noting that $\Delta + \phi$ is the potential of the collector with respect to the plasma, we see that the collector behaves like an ordinary repelling probe (a Druyvesteyn relation holds) when it is repulsive with respect to the plasma, despite the fact that there is an attracting grid before it. On the other hand, the collector behaves like a small attractive spherical probe when it is attractive with respect to the plasma. That is, the current rises linearly, according to (6-9).

Equations (6-7) and (6-8) may be considered as "ideal" relationships. According to the results presented in Ref. 2, (6-8) remains valid for the actual circular planar probe, but (6-7) is modified by the effects of intersections. In the latter case, where $Z < -\phi$, dj/dZ is given by $\exp(-\phi-Z-X_1(Z))$, which is less than unity, instead of (6-7). The function $X_1(Z)$ is greater than $-\phi-Z$ and is the equation of the boundary curve in velocity (X-Z) space separating the domains of allowed and excluded trajectories.

No analytical theory has been developed for off-center points, and (6-6) must be evaluated by trajectory summation. We replace (6-6) by

$$\frac{d}{dZ}\left(\frac{j}{j_o}\right) = \int_{-1}^{1} \frac{db}{2} \int_{-1}^{1} \frac{2dx}{(1-x)^2} \delta e^{-u^2} \tag{6-11}$$

$$\simeq \sum_m \sum_k \frac{H_m H_k}{(1-x_k)^2} \delta_{km} e^{-u_{km}^2} \tag{6-12}$$

where

$$X_k = (1 + x_k)/(1 - x_k) + \mathrm{Max}(0, -\phi - Z) \qquad (6\text{-}13)$$

$$\beta_m = \pi(b_m + 1) \qquad (6\text{-}14)$$

and x_k and b_m are Gaussian quadrature abscissae in the range (-1,1). Also, u^2_{km} is defined by (3-8) and (6-5). If there is no preferred azimuthal plane, we may replace π by $\pi/2$ in (6-14). The Z-derivative of the total current (dI/dZ) may be computed by a sum, over the area, identical to (4-8).

Table 11 gives some computed results for dj/dZ as a function of radius, and dI/dZ, versus Z, for the Mach zero Poisson field (Table 4). The column denoted by "S" gives trajectory step-sizes in cm, and shows the sensitivity of dj/dZ to trajectory accuracy. The columns denoted by dj_1/dZ, dj_2/dZ, and dj_3/dZ give the values of dj/dZ at 3 radii r_1, r_2, and r_3, respectively, which may be compared with dj/dZ at r = 0. Note that dj/dZ falls off with radius. The range of Z is in the neighborhood of the critical value 45.54, where $\phi + Z$ vanishes. A necessary condition for the validity of the Druyvesteyn relation is the validity of (6-8). This implies that dj/dZ (in multiples of j_o) must be equal to unity at Z = 45.54, for all r within the collecting radius. Table 11 shows that at the largest radius, r = 1.48 cm, this is probably not so. (Trajectory step sizes smaller than 0.0125 cm were not used). Morever, Table 11 implies that (6-8) is valid for Z in the vicinity of 45.54, within a small collecting radius. However, for large values of Z, (6-8) probably holds within a larger collecting radius, depending on the value of Z. More computations are required to bear this out. The entries at Z = 40, r = 0, show the sensitivity of dj/dZ to trajectory accuracy (step size), in accord with the exponential dependence on $X_1(Z)$ in velocity space.

Calculations of dj/dZ versus radius are unfortunately not available for the Laplace field, for comparison. Calculations at the central point(2), however, show less sensitivity to trajectory accuracy than those in the Poisson field.

VII. THE ISOLATED SATELLITE. CENTRAL CURRENT IN LAPLACE FIELD.

The calculations described in the preceding sections are based on an infinite-plane model for the satellite. In order to determine the effect of finite satellite size, the satellite was assumed to have the form of a truncated cylinder, at the plasma potential, with the probe disc embedded in one of the circular end-caps. (See Appendix A.)

The difference equations for the isolated satellite are discussed in Appendix A. Figure A-2 illustrates the type of grid used. The Laplace field was computed with a dipole-law condition at the grid boundary. (If the satellite has a net charge, the appropriate condition would include a monopole term.)

The central current density was computed for a number of cases involving a streaming Maxwellian with arbitrary streaming angle. Since the calculation of the current collected by a finite area involves a two-dimensional area integration when the Mach vector is at an angle with respect to the probe normal, a considerable computational saving in time results from evaluating only the central current density. Based on the infinite-satellite results, the central current density represents the collected current to a good approximation, especially in a Laplace field.

Table 12 presents several current-voltage characteristics for the central current density, with various values of M (Mach number) and γ (Mach angle). It is interesting to compare $M = 1.414$, $\gamma = 45°$ with $M = 1$, $\gamma = 0°$. For an infinite-plane (one-dimensional) probe, these curves would be identical, but the slope of the current-voltage characteristic at (1.414, 45°) is, due to 3-dimensional effects, almost twice as great as that at (1, 0°). For numerical consistency, the values of the current at $\phi = 0$ for these two cases, namely 3.54 and 3.62, respectively, should be both equal to 3.64. Thus, the error in the current is of the order of a few percent. Similarly, the cases (1, 90°) and $M = 0$ should give equal currents $\phi = 0$, namely, 1.0. The actual values, namely 0.980 and 0.999, again indicate errors of the order of a few percent. It is also interesting that increasing the Mach number from M = 1 to M = 1.414, at $\gamma = 45°$, produces relatively small changes in the current.

The method used for computing the central current densities in Table 12 is radically different from that used in the infinite-satellite case in that an attempt is made to determine with high accuracy the boundary in velocity space. For each energy in the energy sum (Appendix B or Equation (4-3)), the critical polar angle is found by a systematic search whereby the interval containing the critical angle is successively reduced. Once the critical angle is found, the energy sum (e.g., in (4-3)) can be performed over the occupied range alone, thus avoiding the numerical disadvantage of having to integrate through a step-function where the position of the singularity is not known. It has been found that considerable trajectory accuracy is required if one is to save computer time and use as few trajectories as possible. To obtain the results shown in Table 12, only 8 energies were used. The figures in parentheses in the M = 0 column represent calculations with improved trajectory accuracy.

According to Table 12, the current density at $\phi = -45.54$, M = 1, $\gamma = 0°$, is 82.4, by interpolation, in multiples of the current at zero potential and Mach zero. It is equivalent to 22.6 in multiples of the current at zero potential and Mach 1 (factor 3.64). In Table 3 (Sec. IV), the current at Mach 1, in multiples of the current at zero potential and Mach 1, is 15.6. These two numbers should be identical, but they are obtained by using different methods and different numbers of trajectories.

With respect to computing efficiency, it is not yet clear whether the search method is superior to the "old" method of straight summation (across the singularity). More research is required on this point.

VIII. PHOTOELECTRIC CONTRIBUTIONS

The isolated satellite program was modified to allow the calculation of contributions to the central current density due to photoelectrons or secondary electrons. Whereas (3-12) was used (Sec. VII) to calculate the current density due to a Maxwellian at infinity, (3-13) must instead be used for electron currents from the satellite surface.

For the monoenergetic electrons from the satellite surface, (3-13) becomes

$$j_s = (1 - \Phi/E_o) \iint\limits_{S\ \text{(hemisphere)}} j_{so}(\vec{r}_s)\, \frac{\cos\alpha\ \sin\alpha\ d\alpha\ d\beta}{\pi} \qquad (8\text{-}1)$$

where Φ is the probe potential relative to the emitting (satellite) surface potential, E_o is the singular kinetic energy of the emitted electrons, and $j_{so}(\vec{r}_s)$ is the normal component of the current density of emitted particles at the point $\vec{r}_s$ where the trajectory terminates (originates). Clearly, (8-1) includes only those trajectories which connect the probe with other portions of the satellite surface.

Consider photoelectron contributions alone. Secondary electron currents may be computed in very similar fashion. Let γ_s be the solar angle with respect to the probe normal (satellite axis). Thus $\gamma_s = 0°$ denotes solar radiation parallel to the probe axis and incident normally on the probe; the circular (top) end-cap of the satellite in which the probe is embedded also has solar radiation incident normally at all points, whereas the rest of the satellite receives no radiation. For $\gamma_s = 90°$, only (one-half of) the side surface of the satellite is illuminated. For $\gamma_s = 180°$, only the bottom end-cap (away from the probe) is illuminated. We assume that $j_{so}(\vec{r}_s)$ is proportional to the cosine of the angle between the direction of incidence of solar radiation and the direction of the surface normal at $\vec{r}_s$.

In the axially symmetric Laplace field, every trajectory passing through the central point of the probe lies in a vertical plane containing the probe (and satellite) axis. That is, the azimuthal angle β for the velocity vector of a trajectory at the central point also defines the azimuthal position of the point $\vec{r}_s$ on the satellite where the trajectory terminates. We let the solar direction define azimuth zero. Then, for given values of α and β in (8-1), we follow the trajectory until it reaches the point $\vec{r}_s$ on the satellite surface. The formula for $j_{so}(\vec{r}_s)$ depends on whether $\vec{r}_s$ is on the top (probe), side, or bottom satellite surfaces, and may be expressed as:

$$j_{so}(\vec{r}_s)/j_o = \mathrm{Max}(0, \cos\gamma_s) \qquad \text{(top)} \qquad (8\text{-}2)$$

$$= \mathrm{Max}(0, -\cos\gamma_s) \qquad \text{(bottom)} \qquad (8\text{-}3)$$

$$= \sin\gamma_s \cos\beta \qquad \text{(side)} \qquad (8\text{-}4)$$

where j_o is defined as the emitted photocurrent density for normal solar incidence (which may also be a function of $\vec{r}_s$). The right-hand sides of (8-2) and (8-3) imply that non-zero contributions occur only if $\gamma_s < 90°$ (top illuminated) or if $\gamma_s > 90°$ (bottom illuminated), respectively.

Thus, assuming α_c defines the critical polar angle such that all trajectories with $\alpha > \alpha_c$ return to the satellite, we express (8-1), in view of (8-2) - (8-4), as:

$$j_s/j_o = (1 - \phi) \int_{\sin^2\alpha_c}^{1} d(\sin^2\alpha)\ \mathrm{Max}\ (W, 0)\ \delta \qquad (8\text{-}5)$$

where $\phi \equiv \Phi/E_o$,

$$W = \cos\gamma_s \qquad \text{(top)} \qquad (8\text{-}6)$$

$$= -\cos\gamma_s \qquad \text{(bottom)} \qquad (8\text{-}7)$$

$$= (\sin\gamma_s)/\pi \qquad \text{(side)} \qquad (8\text{-}8)$$

if $\delta = 0$ if the trajectory terminates on the probe surface. In Gaussian summation form, (8-5) becomes

$$\frac{j_s}{j_o} \cong (1 - \phi) \frac{(1 - \sin^2\alpha_c)}{2} \sum_n H_n \text{ Max } (W_n, 0)\, \delta_n \qquad (8\text{-}9)$$

where

$$(\sin^2\alpha)_n = \frac{1}{2} (1 + a_n) + \frac{1}{2} (1 - a_n) \sin^2\alpha_c \qquad (8\text{-}10)$$

and H_n and a_n are corresponding Gaussian coefficients and abscissae.

In the running of trajectories in the Laplace field, the field defined by (4-1) is scaled so that ϕ appears on the probe surface (that is, E_o is the scale of energy). Velocities are defined in multiples of $(2E_o/m)^{1/2}$, so that the initial dimensionless velocity magnitude is $(1 - \phi)^{1/2}$, and the initial polar angle α_n for the n-th trajectory is obtained from (8-10). Some computed results are given in Table 13, for a fixed probe voltage of 15 volts (negative potential energy for electrons), and electron energies of 0.1, 1.0, and 5 volts. Thus, the scaled dimensionless potential energy on the probe was ϕ = -150, -15, and -3, respectively.

In the upper half of Table 13, calculated current densities are given, for solar angles 0°, 35°, 45°, and 90°. The currents fall off with increasing solar angle. At $\gamma_s = 90°$, there are no contributions, since all trajectories terminate on the non-illuminated upper (probe) surface, and none on the illuminated side surface.

The terminal points of a group of trajectories which can contribute are shown in the lower half of Table 13, for each energy. The critical angle α_c increases with electron energy. The quantities x_s represent the x-component of $\vec{r}_s$. The negative value of x_s for the first entry under $E_o = 0.1$ volt occurs because the electron has reversed the direction of its horizontal component of velocity and passed across the axis before returning to the satellite.

APPENDIX A. DIFFERENCE EQUATIONS

A.1. The Infinite-Satellite Equations

When the Poisson partial differential equation in cylindrical polar form is replaced by difference equations in an axially symmetric problem, a grid in r-z space is defined (r is the cylindrical radial coordinate, and z is the axial coordinate). The values of the potential (ϕ) at the grid points, or nodes, are given by the solution of N simultaneous equations in N unknowns, where N is the number of nodes. In the case of a "floating" boundary, some of the nodes are on the boundary. The grid in the present program is bounded by cylindrical surfaces (of constant r and constant z), where the potentials are assumed to obey a dipole law. An exception is the case of a zero-potential boundary (Appendix E).

Figure A-1 illustrates one of the grids employed for the infinite-satellite problem. There are 6 intervals in r and in z, with r_7 defining the radial boundary, and z_7 defining the axial boundary. There are 42 unknown values of potential above the satellite. Of these, 12 are at boundary points where the potential floats, and 5 are interior axial points. The probe surface is defined by r_1, r_2, and r_3 at $z_1 = 0$. The probe potential is ϕ_p. The satellite surface, where $\phi = 0$, is defined by $r_4 - r_7$ at $z_1 = 0$. The potential is defined to be $\phi_p/2$ at the probe radius r_3. On the boundaries, the potentials are assumed to satisfy the linear law:

$$\frac{\partial \phi}{\partial n} = \frac{\partial \phi}{\partial z} = \alpha\phi \qquad \text{on z-boundary} \qquad (A-1)$$

$$\frac{\partial \phi}{\partial n} = \frac{\partial \phi}{\partial r} = \beta\phi \qquad \text{on r-boundary} \qquad (A-2)$$

where n is the outward-directed normal. For the dipole,

$$\alpha = - (2z^2 - r^2)/(r^2 + z^2)/z \qquad \text{(A-3)}$$

$$\beta = - 3r/(r^2 + z^2) \qquad \text{(A-4)}$$

The Laplacian operator may be differenced directly. However, symmetric equations are guaranteed if one differences instead the equivalent divergence theorem (Varga, "Matrix Iterative Analysis"), namely,

$$\iiint_\tau \nabla^2 \phi d\tau = - \iiint \rho d\tau = \iint_\Sigma \frac{\partial \phi}{\partial n} d\Sigma \qquad \text{(A-5)}$$

where ρ is the charge density, $d\tau$ is an element of volume, $d\Sigma$ is an element of area of the surface Σ surrounding the volume τ, and $\partial\phi/\partial n$ is the normal component of grad ϕ at $d\Sigma$. Equation (A-5) is applied to a small volume surrounding each grid point in Fig. A-1. Each small volume is a torus of rectangular cross-section. There are 6 types of equation, exemplified by the points numbered 15, 18, 21, 36, 39, and 42, their associated volumes being marked by shaded boxes.

Each point, axial points excepted, is associated with a volume which has 4 surfaces, e.g., the north, south, east, and west surfaces. Axial points do not have "western" surfaces. The difference equivalent of (A-5) is, for completely interior points (neither on the axis nor on the boundary, such as No. 18):

$$A_N (\partial\phi/\phi n)_N + A_S (\partial\phi/\partial n)_S + A_E (\partial\phi/\partial n)_E + A_W (\partial\phi/\partial n)_W = - \rho\tau \qquad \text{(A-6)}$$

where $(\partial\phi/\partial n)_N$ is approximated by $(\phi_N - \phi) / |z_N - z|$, where ϕ is the central potential (at the point on which the difference equation is centered), ϕ_N is the potential of the neighbor to the north, and z_N is its z-coordinate; and similarly for S, E, and W. In (A-6), the quantities A_N, A_S, A_E, and A_W are the areas of the 4 surfaces, defined by taking sections half-way between grid points. For axial points, the term with subscript W is absent. For points on the z-boundary, the term with subscript N is replaced by $A_N\alpha\phi$, where A_N is the northern area containing the central point. For points on the r-boundary, the term with subscript E is replaced by $A'_E\beta\phi$, where A'_E is the eastern surface area containing the central point. Finally, for points just above the probe and satellite surface, the term with subscript S will contain the known potential.

To illustrate how the equations are formed, we obtain from (A-6) the following equations for the exemplary points in Fig. A-1.

Point 18 (interior)

$$C_N \phi_{25} + C_S \phi_{11} + C_E \phi_{19} + C_W \phi_{17}$$

$$- (C_N + C_S + C_E + C_W) \phi_{18} = - \rho_{18}\tau_{18} \quad \text{(A-7)}$$

where

$$C_N = A_N / (z_5 - z_4) \quad \text{(A-8)}$$

$$A_N = (\pi/4) [(r_5 + r_4)^2 - (r_4 + r_3)^2] \quad \text{(A-9)}$$

$$C_S = A_N / (z_4 - z_3) \quad \text{(A-10)}$$

$$C_E = A_E/(r_5 - r_4) \tag{A-11}$$

$$A_E = (\pi/2)\ (r_5 + r_4)\ (z_5 - z_3) \tag{A-12}$$

$$C_W = A_W/(r_4 - r_3) \tag{A-13}$$

$$A_W = (\pi/2)\ (r_4 + r_3)\ (z_5 - z_3) \tag{A-14}$$

$$\tau_{18} = (z_5 - z_3)\ A_N/2 \tag{A-15}$$

<u>Point 15 (axial)</u>

$$C_N\ \phi_{22} + C_S\ \phi_8 + C_E\ \phi_{16} - (C_N + C_S + C_E)\ \phi_{15} = -\ \rho_{15}\tau_{15} \tag{A-16}$$

where

$$C_N = A_N/(z_5 - z_4) \tag{A-17}$$

$$A_N = (\pi/4)\ r_2^{\ 2} \tag{A-18}$$

$$C_S = A_N/(z_4 - z_3) \tag{A-19}$$

$$C_E = A_E/r_2 \tag{A-20}$$

$$A_E = (\pi/2)\ r_2\ (z_5 - z_3) \tag{A-21}$$

$$\tau_{15} = (z_5 - z_3)\ A_N/2 \tag{A-22}$$

Point 21 (r-boundary)

$$C_N \phi_{28} + C_S \phi_{14} + C_W \phi_{20}$$

$$- (C_N + C_S + C_W - \beta A_E') \phi_{21} = - \rho_{21}\tau_{21} \qquad \text{(A-23)}$$

where

$$C_N = A_N/(z_5 - z_4) \qquad \text{(A-24)}$$

$$A_N = (\pi/4)[4r_7^2 - (r_7 + r_6)^2] \qquad \text{(A-25)}$$

$$C_S = A_N/(z_4 - z_3) \qquad \text{(A-26)}$$

$$A_E' = \pi r_7 (z_5 - z_3) \qquad \text{(A-27)}$$

$$C_W = A_W/(r_7 - r_6) \qquad \text{(A-28)}$$

$$A_W = (\pi/2)(r_7 + r_6)(z_5 - z_3) \qquad \text{(A-29)}$$

$$\tau_{21} = (z_5 - z_3) A_N/2 \qquad \text{(A-30)}$$

Point 36 (z-boundary, axial)

$$C_S \phi_{29} + C_E \phi_{37}$$

$$- (C_S + C_E - \alpha A_S) \phi_{36} = - \rho_{36}\tau_{36} \qquad \text{(A-31)}$$

where

$$C_S = A_S/(z_7 - z_6) \tag{A-32}$$

$$A_S = (\pi/4)\ r_2^{\ 2} \tag{A-33}$$

$$C_E = A_E/r_2 \tag{A-34}$$

$$A_E = (\pi/2)\ r_2\ (z_7 - z_6) \tag{A-35}$$

$$\tau_{36} = (z_7 - z_6)\ A_S/2 \tag{A-36}$$

<u>Point 39 (z-boundary)</u>

$$\begin{aligned} &C_S\ \phi_{32} + C_E\ \phi_{40} + C_W\ \phi_{38} \\ &\qquad - (C_S + C_E + C_W - \alpha A_S)\ \phi_{39} = -\ \rho_{39}\tau_{39} \end{aligned} \tag{A-37}$$

where

$$C_S = A_S/(z_7 - z_6) \tag{A-38}$$

$$A_S = (\pi/4)\ [(r_5 + r_4)^2 - (r_4 + r_3)^2] \tag{A-39}$$

$$C_E = A_E/(r_5 - r_4) \tag{A-40}$$

$$A_E = \pi\ (r_5 + r_4)(z_7 - z_6) \tag{A-41}$$

$$C_W = A_W/(r_4 - r_3) \tag{A-42}$$

$$A_W = \pi \, (r_4 + r_3)(z_7 - z_6) \tag{A-43}$$

$$\tau_{39} = (z_7 - z_6) \, A_S/2 \tag{A-44}$$

Point 42 (z-boundary, r-boundary)

$$C_S \, \phi_{35} + C_W \, \phi_{41}$$

$$- (C_S + C_W - \alpha A_S - \beta A_E') \, \phi_{42} = - \rho_{42} \tau_{42} \tag{A-45}$$

where

$$C_S = A_S/(z_7 - z_6) \tag{A-46}$$

$$A_S = (\pi/4) \, [4r_7^2 - (r_7 + r_6)^2] \tag{A-47}$$

$$A_E' = \pi r_7 \, (z_7 - z_6) \tag{A-48}$$

$$C_W = A_W/(r_7 - r_6) \tag{A-49}$$

$$A_W = (\pi/2)(r_7 + r_6)(z_7 - z_6) \tag{A-50}$$

$$\tau_{42} = (z_7 - z_6) \, A_S/2 \tag{A-51}$$

It is clear that the N x N matrix of coefficients will be symmetric, since the coefficients of the off-diagonal elements are simply the areas of the interfaces divided by the length of the segment joining the adjacent grid points. It is also clear that where α and β are both negative, which is the case for a reasonable boundary shape, the matrix is diagonally dominant. This is important for iterative solution methods.

For grid points in the row next to the probe and satellite surfaces, such as points Nos. 1-7 in Fig. A-1, the off-diagonal terms with subscript S will be absent from the left-hand side of the equation, but will instead be added to the right-hand side as known quantities. For the Laplace problem, when ρ vanishes, these latter contributions constitute the only source of the potential.

In the dipole-boundary calculations reported in the main text for the infinite-satellite case, the equations for the axial points were based on a quadratic relation rather than equations typified by (A-16) - (A-22), for point No. 15. Thus, densities were not required for these points (Sec. V), and therefore the Poisson potentials do not contain axial density information. (The zero-potential-boundary calculations of Appendix E do utilize the axial point equations of this Appendix.) The error resulting from the lack of axial density information is not known; the quadratic relation has merit in that it tends to smooth out potential variations due to computational "noise", and has been suggested by Collatz ("The Numerical Treatment of Differential Equations"). The equations used for the infinite-satellite problem included additional equations at the boundary points. These involved the tangential component of the potential gradient. The additional equations therefore resulted in an overdetermined system, to which solutions were obtained in a least-squares sense. It is felt, however, that the equations of this Appendix, which have been recently developed, are preferable.

A.2. The Isolated-Satellite Equations

Figure A-2 illustrates the type of grid used for the finite satellite having the form of a truncated cylinder. The geometry is still cylindrical polar, but the space of the problem is conveniently separated into three regions, i.e., North, East, and South, illustrated by 24 points in Fig. A-2. Each of the three regions may then be described by rectangular grids similar to those in Fig. A-1, except that the z-coordinates of the grid lines are numbered in order from top to bottom rather than from bottom to top. The probe is embedded in the North circular end-cap of the satellite. The probe and satellite potentials are ϕ_p and zero, respectively, as before.

The equations are derived in a manner identical to those of the previous section. The shaded boxes in Fig. A-2 represent, as before, toroidal boxes of rectangular cross-section. Point No. 9 is an interior point similar to No. 18 in Fig. A-1, and points Nos. 1, 3, 5, 6, and 14 correspond similar to points Nos. 36, 39, 42, 15, and 21 in Fig. A-1, respectively. There is an additional z-boundary, on the southern side. At this surface, the relation between $\partial\phi/\partial n$ and ϕ is $\partial\phi/\partial n = -\alpha\phi$, with α given by (A-3). The equations are obtained from (A-6), as before; one notes, however, that whereas terms with subscripts S appear in the equations for points along the northern z-boundary, corresponding terms at the southern z-boundary have subscripts N.

A.3 Solution of the Linear Equations

Considering the charge densities as known along with the satellite and probe potentials (as in one cycle of self-consistent iteration), the equations given above may be expressed in the matrix-vector form:

$$A\vec{\phi} = \vec{k} \qquad \text{(A-52)}$$

Here, A denotes the matrix of coefficients, $\vec{\phi}$ denotes the N-dimensional solution-vector, and $\vec{k}$ denotes the known vector. This system can be solved either by direct or by iterative methods. The direct method may be quite efficient, despite large values of N, since A can be partitioned in block-tridiagonal form and solutions obtained by methods based on tridiagonal matrices (by factorization, as discussed by Varga in "Matrix Iterative Analysis"). This method involves rather complicated programming but does not depend on the properties of the matrix.

On the other hand, since the matrix A is symmetric and diagonally dominant, over-relaxation methods can be used (see Varga) which are extremely simple to program. Briefly, the over-relaxation algorithm may be expressed by the equations:

$$- a_{ii}\psi_i^{n+1} = \sum_{j=1}^{i-1} a_{ij}\phi_j^{n+1} + \sum_{j=i+1}^{N} a_{ij}\phi_j^{n} \qquad \text{(A-53)}$$

$$\phi_i^{n+1} = \omega\, \psi_i^{n+1} + (1 - \omega)\, \phi_i^{n} \qquad \text{(A-54)}$$

In these equations, a_{ij} denotes the (i, j)-th element of A, the superscipts n and n+1 denote the n-th and (n+1)-th iterates, respectively, and ω is the relaxation parameter which is assigned a value between 1 and 2.

For a 636-point problem involving the Laplace field, where the initial guess was $\vec{\phi} = 0$, the number of iterations required to obtain convergence within 1 part in 10^5 was greater than 2000 for $\omega = 1.0$, 1733 for $\omega = 1.2$, 144 for $\omega = 1.9$, and infinity for $\omega = 2.0$. This shows the vital role played by ω. At $\omega = 1.9$, which is apparently the optimum value, only about 20 seconds were required on the CDC-6400 computer. This is clearly competitive with 30 seconds for the direct solution, which required a great deal longer to program and de-bug.

APPENDIX B. TRAJECTORY QUADRATURE SUMS

The triple integrals for the density and the current density components, defined by (2-1) and (2-2), may be expressed in the polar form

$$n = \iiint f \, d^3 \vec{v}$$

$$= \frac{1}{2} \left(\frac{2E_o}{m} \right)^{3/2} \iiint f(E,\alpha,\beta)(E-\phi)^{1/2} \, dE \sin\alpha \, d\alpha \, d\beta \tag{B-1}$$

and

$$j = \iiint f \, v_z \, d^3 \vec{v}$$

$$= \frac{2E_o^2}{m^2} \iiint f(E,\alpha,\beta) \, (E-\phi) \, dE \sin\alpha \cos\alpha \, d\alpha \, d\beta \tag{B-2}$$

with

$$E = \frac{mv^2}{2E_o} + \phi \tag{B-3}$$

where E_o is a characteristic energy, E denotes the dimensionless kinetic energy of the particle at its source, ϕ denotes the local dimensionless potential energy of the particle (relative to the source), and α and β denote the angular coordinates of the local velocity vector, namely, the polar angle with respect to an axis and the azimuthal angle with respect to a plane, respectively. The angular integration ranges are defined to be only over those values for which trajectories connect with the emitter, e.g., infinity. Defining the polar axis to be in the direction of the normal to a collecting surface, as in Fig. 2, the component of current density normal to the surface is given by (B-2). The order of integration depends on the function $f(E,\alpha,\beta)$. In the usual probe theory, the angular integrations are performed first, and the energy last. In special situations, such as photoelectric emission, however, it may be necessary to perform the angular integrations last. (See 3-10) and (3-13).) In the following, the usual order will be assumed for illustration, without affecting the general validity of the formulae.

In the α integration, the range is π in (B-1), and $\pi/2$ in (B-2). In the energy integration, the range is usually infinite. In order to deal with this, it is convenient to transform the energy variable thus:

$$E = (1 + A)/(1 - A) + E_{min} \qquad \text{(B-4)}$$

where A runs from -1 to 1 as E runs from its minimum value E_{min} to infinity.

The density and current density can be expressed in dimensionless form by dividing (B-1) by

$$n_o = \frac{1}{2}\left(\frac{2E_o}{m}\right)^{3/2} \iiint f(E,\alpha,\beta)E^{1/2}\, dE \sin\alpha\, d\alpha\, d\beta \qquad \text{(B-5)}$$

$$= \frac{1}{2}\left(\frac{2E_o}{m}\right)^{3/2} 4\pi \int_o^\infty f(E)\, E^{1/2}\, dE \qquad \text{(B-6)}$$

and (B-2) by

$$j_o = \frac{2E_o^{\;2}}{m^2}\iiint f(E,\alpha,\beta)\ E\ dE\ \sin\alpha\ \cos\alpha\ d\alpha\ d\beta \qquad \text{(B-7)}$$

$$= \frac{2E_o^{\;2}}{m^2}\ \pi \int_o^\infty f\ (E)\ E\ dE \qquad \text{(B-8)}$$

where (B-6) and (B-8) imply isotropic distributions (which are less complicated but not essential). Then we have

$$\frac{n}{n_o} = \iiint F(E)(E-\phi)^{1/2}\ dE\ \frac{\sin\alpha\ d\alpha\ d\beta}{4\pi} \qquad \text{(B-9)}$$

and

$$\frac{j}{j_o} = \iiint G(E)(E-\phi)\ dE\ \frac{\sin\alpha\ \cos\alpha\ d\alpha\ d\beta}{\pi} \qquad \text{(B-10)}$$

where F and G have the non-dimensional definitions:

$$F(E) = f(E) \div \int_o^\infty f(E)\ E^{1/2}\ dE \qquad \text{(B-11)}$$

and

$$G(E) = f(E) \div \int_o^\infty f(E)\ E\ dE \qquad \text{(B-12)}$$

In (B-9), α and β lie in the ranges $(0,\pi)$ and $(0,2\pi)$, respectively. With (B-4) and the transformations

$$\cos\alpha = B \tag{B-13}$$

and

$$\beta = \pi(C+1) \tag{B-14}$$

we may express (B-9) in the form:

$$\frac{n}{n_o} = \int_{-1}^{1}\int_{-1}^{1}\int_{-1}^{1} \frac{1}{2} F\,[E(A)]\,[E(A)-\phi]^{1/2}\,\delta\,\frac{dA\,dB\,dC}{(1-A)^2} \tag{B-15}$$

where δ is the unit step-function.

In (B-10), α and β lie in the ranges $(0,\pi/2)$ and $(0,2\pi)$, respectively. With (B-4), (B-14), and the transformation

$$\sin^2\alpha = (1+B)/2 \tag{B-16}$$

we may express (B-10) in the form:

$$\frac{j}{j_o} = \int_{-1}^{1}\int_{-1}^{1}\int_{-1}^{1} \frac{1}{2} G\,[E(A)]\,[E(A)-\phi]\,\delta\,\frac{dA\,dB\,dC}{(1-A)^2} \tag{B-17}$$

where δ is the unit step-function, as usual.

Now we have the integrals, (B-15) and (B-17), in the form suitable for Gaussian quadratures. Let A_j, H_j be the j-th abscissa and coefficient in a Gaussian quadrature of order N. There are N such pairs. Then A_1, A_2, ... A_N lie in the interval (-1, 1), and the sum of the H_j is 2. For flexibility, we divide the A-range into M_1 sub-intervals, and apply a Gaussian quadrature of order N_1 to each of these. We divide the B-range into M_2 sub-intervals and apply a Gaussian quadrature of order N_2 to each of these. We divide the C-range into M_3 sub-intervals and apply a Gaussian quadrature of order N_3 to each of these. Then either (B-15) or (B-17) may be approximated by the 6-fold sum:

$$I = \int_{-1}^{1}\int_{-1}^{1}\int_{-1}^{1} T\,(A,B,C)\ \delta\ dA\ dB\ dC$$

$$\simeq \frac{1}{M_1\ M_2\ M_3} \sum_{K=1}^{M_1} \sum_{k=1}^{N_1} \sum_{J=1}^{M_2} \sum_{j=1}^{N_2} \sum_{I=1}^{M_3} \sum_{i=1}^{N_3} H_k^{(1)}\ H_j^{(2)}\ H_i^{(3)}\ T(U,V,W)\ \delta \qquad \text{(B-18)}$$

where δ is the unit step-function, and U, V, and W are defined by

$$U = (A_k - 1 - M_1 + 2K)/M_1 \qquad \text{(B-19)}$$

$$V = (B_j - 1 - M_2 + 2J)/M_2 \qquad \text{(B-20)}$$

$$W = (C_i - 1 - M_3 + 2I)/M_3 \qquad \text{(B-21)}$$

and (C_i, $H_i^{(3)}$), (B_j, $H_j^{(2)}$), and (A_k, $H_k^{(1)}$) are associated Gaussian abscissa-coefficient pairs.

In all of the calculations reported here, I used $M_1 = 2$, $M_2 = M_3 = 1$. In the density calculations, $N_1 = N_2 = N_3 = 8$. In the most accurate current density calculations, for the central point, $N_1 = N_2 = 32$.

Based on the experience of the present investigation, I recommend the use of low-order Gaussian quadratures, with large numbers of intervals. This should be most efficient for the integration of a step-function integrand. In the case $N_1 = N_2 = N_3 = 2$, the coefficients are $H_1 = H_2 = 1$, and the abscissae are $A_1 = -A_2 = -3^{-1/2}$.

For the current-derivative dj/dZ, which requires a two-dimensional sum as shown in Sec VI, a two-fold analogue of (B-18) may be employed.

Each term in the multiple sum (B-18) corresponds to a single trajectory. This trajectory is defined by the local position and velocity. The local velocity components may be obtained in cartesian form from (B-4), (B-14), and either (B-13) for density or (B-16) for current. Thus, the dimensionless cartesian components are given, for density and current, respectively, by:

$$v_x/v = (1 - V^2)^{1/2} \cos\pi(1 + W) \quad \text{or} \quad ((1 + V)/2)^{1/2} \cos\pi(1 + W) \tag{B-22}$$

$$v_y/v = (1 - V^2)^{1/2} \sin\pi(1 + W) \quad \text{or} \quad ((1 + V)/2)^{1/2} \sin\pi(1 + W) \tag{B-23}$$

$$v_z/v = V \quad \text{or} \quad ((1 - V)/2)^{1/2} \tag{B-24}$$

$$v = [(1 + U)/(1 - U) + E_{min} - \phi]^{1/2} \tag{B-25}$$

where U, V, and W are defined by (B-19) - (B-21).

APPENDIX C. EQUATIONS OF MOTION. TRAJECTORIES.

If X, Y, Z, and V_x, V_y, and V_z denote dimensional spatial and velocity cartesian coordinates, respectively, and if T and Φ denote dimensional time and potential energy, respectively, then Newton's equations of motions are:

$$\frac{d^2X}{dT^2} = -\frac{1}{m}\frac{\partial\Phi}{\partial X} \qquad \text{(C-1)}$$

$$\frac{d^2Y}{dT^2} = -\frac{1}{m}\frac{\partial\Phi}{\partial Y} \qquad \text{(C-2)}$$

$$\frac{d^2Z}{dT^2} = -\frac{1}{m}\frac{\partial\Phi}{\partial Z} \qquad \text{(C-3)}$$

where m is the particle mass.

Now choose the following units:

R_o = unit of length

T_o = unit of time

E_o = unit of energy

$V_o = R_o/T_o = (2E_o/m)^{1/2}$ = unit of velocity

and let the following variables represent dimensionless quantities:

$x, y, z = X/R_o, Y/R_o, Z/R_o$ (dimensionless position)

$t = T/T_o$ (dimensionless time)

$\phi = \Phi/E_o$ (dimensionless potential energy)

$v_x, v_y, v_z = V_x/V_o, V_y/V_o, V_z/V_o$ (dimensionless velocity)

Then the equations of motion have the dimensionless form:

$$\frac{d^2x}{dt^2} = - \frac{1}{2} \frac{\partial \phi}{\partial x} \qquad (C\text{-}4)$$

$$\frac{d^2y}{dt^2} = - \frac{1}{2} \frac{\partial \phi}{\partial y} \qquad (C\text{-}5)$$

$$\frac{d^2z}{dt^2} = - \frac{1}{2} \frac{\partial \phi}{\partial z} \qquad (C\text{-}6)$$

In the Laplace problem, the unit of length is arbitrary, but in the Poisson problem, it is most conveniently set equal to the Debye length $(kT/4\pi n_o e^2)^{1/2}$. The unit of energy is kT, and the unit of velocity is $(2kT/m)^{1/2}$, in the calculations reported here for the Maxwellian distribution. For each trajectory, the initial velocity components are usually specified by the quadrature indices, as in Appendix B.

The equations of motion (C-4) - (C-6) are integrated over successive time intervals of length Δt to obtain new values for the coordinates x, y, z, and the velocities $\dot{x}$, $\dot{y}$, and $\dot{z}$. During each time interval, the accelerations, i.e., the potential gradient components, are assumed constant. Thus, the changes in x, y, z, and $\dot{x}$, $\dot{y}$, and $\dot{z}$ are given rather crudely by truncated Taylor series, namely:

$$\Delta x = \dot{x}_o \Delta t + \ddot{x}_o (\Delta t)^2/2 \qquad (C\text{-}7)$$

$$\Delta y = \dot{y}_o \Delta t + \ddot{y}_o (\Delta t)^2/2 \qquad (C\text{-}8)$$

$$\Delta z = \dot{z}_o \Delta t + \ddot{z}_o (\Delta t)^2/2 \qquad (C\text{-}9)$$

$$\Delta \dot{x} = \ddot{x}_o \Delta t \qquad (C\text{-}10)$$

$$\Delta \dot{y} = \ddot{y}_o \Delta t \qquad (C\text{-}11)$$

$$\Delta \dot{z} = \ddot{z}_o \Delta t \qquad (C\text{-}12)$$

where the zero-subscripts denote the values of the quantities at the beginning of the time interval. The use of a crude rather than a sophisticated integration scheme is based on the fact that the potential distribution is given in the form of a grid and the gradients are therefore discontinuous across the grid lines. A high-order scheme is defeated by these discontinuities and its computational expense appears to be unjustified.

The required gradient components in (C-4) - (C-6) are obtained by double linear interpolation within the boxes of the two-dimensional array in r and z, as follows. Let $\phi(i, j)$ denote the value of ϕ at the point (z_i, r_j). Assume that z and r are located in the ranges $z_i \leq z < z_{i+1}$ and $r_j \leq r < r_{j+1}$, respectively, and let $z_{i+1} - z_i$ and $r_{j+1} - r_j$ be denoted by D_z and D_r, respectively. Then the interpolated values of $\partial\phi/\partial z$ and $\partial\phi/\partial r$ are given by:

$$\partial\phi/\partial z = [\phi(i+1, j) - \phi(i, j)]/D_z + (r-r_j)Q/(D_r D_z) \qquad (C\text{-}13)$$

$$\partial\phi/\partial r = [\phi(i, j+1) - \phi(i, j)]/D_r + (z-z_i)Q/(D_r D_z) \qquad (C\text{-}14)$$

where

$$Q = \phi(i+1, j+1) - \phi(i, j+1) - \phi(i+1, j) + \phi(i, j) \qquad (C\text{-}15)$$

The cartesian gradient components $\partial\phi/\partial x$ and $\partial\phi/\partial y$ are then given by:

$$\partial\phi/\partial x = (x/r)\ \partial\phi/\partial r \qquad \text{(C-16)}$$

$$\partial\phi/\partial y = (y/r)\ \partial\phi/\partial r \qquad \text{(C-17)}$$

The above interpolation scheme is easily modified to allow for a grid in which increasing values of i are associated with decreasing values of z, such as was employed in the isolated satellite program.

The trajectory accuracy is related to the length of the step, since the gradient is not constant during a step. The type of step control which was used during these investigations maintained an approximate equality of arc length per step throughout the trajectory. If Δs is the desired controlled value of step length, then setting Δt equal to $\Delta s/(\dot{x}_o^2 + \dot{y}_o^2 + \dot{z}_o^2)^{1/2}$ accomplishes this control. This assumes that the accleration term in the equations is always dominated by the velocity term. The maintenance of equal arc length per step is wasteful, however, in the outer regions of the potential grid, where the potential gradients are small. A better procedure would be to use energy-conservation control.

A convenient indicator of the accuracy of a trajectory is the degree to which energy is conserved. Numerical errors occur because the force changes during Δt, and equations (C-7) - (C-12) result in an energy loss or gain at the end of the step. If $c \equiv |\Delta E|/E$ is the desired maximum relative energy loss or gain per step, a useful and fairly conservative control would be given by

$$\Delta t = \mathrm{Min}\ (T_1, T_2) \qquad \text{(C-18)}$$

where

$$T_1 = cE/(pq) \tag{C-19}$$

$$T_2 = (cE)^{1/2}/p \tag{C-20}$$

$$p = |\partial\phi/\partial x| + |\partial\phi/\partial y| + |\partial\phi/\partial z| \tag{C-21}$$

$$q = |\dot{x}_o| + |\dot{y}_o| + |\dot{z}_o| \tag{C-22}$$

This type of control has the advantage of allowing the step size to be large in regions of weak forces, while "tightening up" in regions where the force is strong. Thus, a large number of step size tests (see Appendix E, for example) can be eliminated.

In order to determine the "fate" of a trajectory, it is followed until it either returns to the satellite surface, or passes through the outer grid boundary. If it reaches the boundary, it is considered to have escaped. However, on reaching the r-boundary in the infinite-satellite case, the velocity vector must be extrapolated (zero field) to see whether the particle escapes or not. This amounts simply to examining the sign of v_z.

APPENDIX D. ITERATION PROCEDURES

According to Sec. V and Appendix A, the set of Poisson difference equations representing the Poisson partial differential equation on a grid may be expressed as a matrix-vector equation for an N-component solution vector $\vec{\phi}$ as follows:

$$L\vec{\phi} = \vec{F}\,(\vec{\phi}) \qquad \text{(D-1)}$$

In (D-1), L is the Laplacian matrix operator, and $\vec{F}$ is the corresponding net negative charge density vector, each component of which depends in general on more than one component of $\vec{\phi}$. Given a computational algorithm for finding $\vec{F}$ when $\vec{\phi}$ is given (Appendices B and C), we must use an iterative technique to obtain a self-consistent solution.

The simplest iteration, where n denotes the iteration index, is the direct one, namely,

$$L\,\vec{\phi}_{n+1} = \vec{F}\,(\vec{\phi}_n) \qquad \text{(D-2)}$$

where $\vec{\phi}_0$ might, for example, be the Laplace solution. The direct iteration defined by (D-2) may converge or diverge, depending on the position of the boundary. In the present investigation, it has been found that if the boundary of the grid is near the probe, the direct iteration will converge, but if the boundary is moved out beyond a certain point, the iteration will diverge. We define that point as the "critical distance". In order to represent a boundary condition at infinity, the boundary must be reasonably far from the probe; actually, it must be sufficiently far that further increases in distance do not affect the computed current (that is, the current becomes stationary). Unfortunately, the distance beyond which the current is stationary is greater than the critical distance for the iteration scheme (D-2).

It has been found possible to increase the critical distance by using a more sophisticated iteration. Thus, an important improvement is afforded by

$$L \vec{\phi}_{n+1} = \vec{F}_{n+1} \tag{D-3}$$

where

$$\vec{F}_{n+1} = \alpha \vec{F} (\vec{\phi}_n) + (1 - \alpha) \vec{F}_n \tag{D-4}$$

The implication of (D-4) is that the next charge density vector to be used consists of an average of (a) the charge density vector resulting from the latest available potential vector, and (b) the charge density vector which was the source of that potential vector. The iteration of (D-3) and (D-4) is equivalent to a heat-diffusion problem with the iteration index n playing the role of time. The reciprocal of α plays the role of a damping constant. This may be seen by re-writing (D-3) and (D-4) in the "relaxation" form:

$$\vec{F}_{n+1} - \vec{F}_n = \alpha [F (\vec{\phi}_n) - L\vec{\phi}_n] \tag{D-5}$$

Thus, the smaller is the value of α, the smaller is the change from iteration to iteration, corresponding to large damping. The mixing or coupling is applied to the charge density, according to (D-4). Alternatively, of course, it may be applied instead to the potential.

In the Poisson calculations reported in Sec. V, the scheme of (D-4) employing $\alpha = 1/2$ worked well when the z-boundary was within 1.5 probe radii, converging within about 6 iterations. However, when the z-boundary was at 3 probe radii, it was necessary to reduce α. Actually, α was defined as $1/n$, i.e., decreasing with increasing iteration number. At 3 probe radii, convergence was achieved within about 12 iterations. A small constant value of α, perhaps 1/10, would probably also have assured convergence.

APPENDIX E. ZERO-POTENTIAL BOUNDARY

A coarse grid with 6 unknown values of potential was used for the Poisson zero-potential boundary calculation, in order to prove that the boundary condition is irrelevant (for current) when the boundary is sufficiently far out. Since this calculation exemplifies all of the Poisson calculations, and because the grid is small, it will be instructive and convenient to present the calculation in detail here.

With probe radius 3.33 cm, identical sets of values were chosen for the radial and axial grid coordinates (infinite satellite, Appendix A), namely:

$$\begin{array}{ll} r_1 = 0 & z_1 = 0 \\ r_2 = 3.33 & z_2 = 3.33 \\ r_3 = 6.66 & z_3 = 6.66 \\ r_4 = 9.99 & z_4 = 9.99 \end{array} \qquad \text{(E-1)}$$

With a probe potential -45.54 in multiples of kT, the zero-order (Laplacian) potential array was calculated, with zero on the boundary, to be as given in Table E-1:

TABLE E-1

Laplace Potential. 4 x 4 Grid

	$r_1 = 0$	$r_2 = 3.33$	$r_3 = 6.66$	$r_4 = 9.99$
$z_4 = 9.99$	0	0	0	0
$z_3 = 6.66$	- 4.56 (#1)	- 3.24 (#2)	- 1.10 (#3)	0
$z_2 = 3.33$	-14.4 (#4)	- 9.04 (#5)	- 1.97 (#6)	0
$z_1 = 0$	-45.54	-22.77	0	0

This solution was calculated using a suitable modification -- actually a simplification -- of the equations of Appendix A. Since the grid is coarse, the potentials are approximate, but are probably not greatly in error.

Let the density at the 6 points, namely, (r_1, z_3), (r_2, z_3), (r_3, z_3), (r_1, z_2), (r_2, z_2), and (r_3, z_2), be designated by n_1, n_2, n_3, n_4, n_5, and n_6, respectively. These represent the 6 components of a density vector. The numbers in parentheses in Table E-1 indicate the geometric ordering of the positions. The potentials at the 6 points will be similarly designated by ϕ_1, ϕ_2, ϕ_3, ϕ_4, ϕ_5, and ϕ_6, constituting the components of a potential vector.

Using 16 values of k, 8 values of ℓ, and 8 values of m in the sum (5-3) of Sec. V, a sequence of step-sizes was employed to find the optimum values. The following sequence of density vectors was computed (at Mach zero) in the Laplace field, as a function of step-size:

TABLE E-2

Densities versus Step-Size

	S = .4	S = .2	S = .1	S = .05	S = .025	S(adopted)
n_1	.0955/.0076	.137/.0076	.179/.0076	.179/.0076		.1
n_2	.175/.0373	.208/.0373	.220/.0373	.226/.0373		.05
n_3	.305/.244	.312/.244	.315/.244	.315/.244		.2
n_4	.0623/0	.217/0	.280/0	.418/0	.598/0	.025
n_5	.292/0	.372/0	.416/0	.431/0	.423/0	.025
n_6	.325/.0610	.363/.0642	.376/.0660	.379/.0666		.05

In Table E-2, the number to the left/right side of each solidus(/) represents the density of attracted/repelled particles, respectively. The adopted step sizes are shown in the last column. Note that the repelled particle densities are insensitive to step size. The attracted-particle density n_4 was most sensitive to step size. Although S = .025 does not represent a small enough step for n_4 (attracted) to become stationary, it was felt to be reasonably accurate in the interest of saving computer time.

An iteration was employed, such as described in Appendix D, with $\alpha = 1/(n + 2)$ and n denoting iteration number. The sequence of potential iterates obtained is shown in Table E-3.

TABLE E-3

Potential Iterates

order =	0th	1st	2nd	3rd	4th	5th	6th
ϕ_1	- 4.56	- 3.54	- 3.29	- 3.17	- 3.11	- 3.07	- 3.05
ϕ_2	- 3.24	- 2.36	- 2.17	- 2.09	- 2.04	- 2.02	- 2.00
ϕ_3	- 1.10	- .642	- .652	- .625	- .615	- .613	- .610
ϕ_4	-14.4	-12.8	-12.4	-12.2	-12.1	-12.0	-12.0
ϕ_5	- 9.04	- 7.73	- 7.38	- 7.24	- 7.16	- 7.11	- 7.08
ϕ_6	- 1.97	- 1.18	- 1.05	- 1.01	- .997	- .990	- .987

The sequence of density iterates (attracted/repelled) obtained is shown in Table E-4.

TABLE E-4

Density Iterates

	0th	1st	2nd	3rd	4th	5th	6th
n_1	.179/.0076	.215/.0276	.217/.0354	.218/.0400	.219/.0425	.219/.0441	.220/.0451
n_2	.226/.0373	.256/.0900	.262/.108	.273/.117	.273/.123	.273/.126	.273/.128
n_3	.315/.244	.315/.362	.350/.343	.356/.352	.356/.356	.357/.357	.357/.358
n_4	.598/0	.481/0	.590/0	.478/0	.478/0	.478/0	.477/0
n_5	.423/0	.447/0	.398/0	.404/0	.403/0	.402.0	.402/0
n_6	.379/.0666	.376/.156	.369/.178	.363/.186	.362/.188	.362/.191	.362/.192

In Table E-4, the 0th-order, 1st-order, etc., densities are computed directly from the potentials under the corresponding columns in Table E-3. The potentials in Table E-3, however, are calculated according to the scheme of Appendix D, so that the actual densities used are linear combinations of those in Table E-4. In fact, using $\alpha = 1/2, 1/3, 1/4,$ etc., when $n = 0, 1, 2,$ etc., in Equation (D-4) of Appendix D, and with $\vec{F}_o = 0$, we obtain ($\vec{F}$ = net negative charge density):

$$\vec{F}_n = \frac{1}{n+1} [\vec{F}(\vec{\phi}_o) + \vec{F}(\vec{\phi}_1) + \ldots \vec{F}(\vec{\phi}_{n-2})] \qquad \text{(E-2)}$$

where $\vec{F}(\vec{\phi}_m)$ is obtained directly from the m-th order column in Table E-4. The n-th order potential ϕ_n is then computed directly from $\vec{F}_n$ as given by (E-2). Thus, $\vec{\phi}_1$ is computed using $1/2\ \vec{F}(\vec{\phi}_o)$, $\vec{\phi}_2$ is computed using $1/3\ \vec{F}(\vec{\phi}_o) + 1/3\ \vec{F}(\vec{\phi}_1)$, etc.

Finally, the central current density is given, as a function of step size, in Table E-5. (Laplace potential from Table E-1, Poisson potential from Table E-3).

TABLE E-5

Current Density

	Laplace	Poisson
S = .1	32.7	--
S = .05	33.5	31.3
S = .025	34.0	33.0

Hence, although there is a tendency for the current to increase with decreasing step size, it is clear that the current densities are quite close to the values given in Table 6 (see Sec. V), namely, 34.0 versus 35.5 for Laplace, and 33.0 versus 33.3 for Poisson

APPENDIX F. NUMERICAL EFFECTS OF BOUNDARY

The role played by the boundary condition was investigated principally by calculating current versus boundary position.

In the Laplace case, with probe potential -45.54 kT at Mach zero, the current was calculated for grids with increasing r-boundary (fixed z-boundary) and for grids with increasing z-boundary (fixed r-boundary). Table F-1 shows that the current is rather insensitive to boundary position.

TABLE F-1

Laplace Current versus (r,z)-boundary

r/a	(z=3a) I/I_o	z/a	(r=3a) I/I_o
2	35	2	32
2.5	35	2.5	33
3	35	3	34/36

The pair of values 34/36 under the r=3a column at z=3a indicates the variation resulting from using 6/12 intervals in z, respectively.

In the Poisson case, with probe potential -45.54 kT at Mach zero, the current was calculated with fixed r-boundary (r=3a), and increasing z-boundary values. Table F-2 shows the results using a coarse grid, with $\Delta r = \Delta z = a$.

TABLE F-2

Poisson Current versus z-boundary

z/a =	1.5	2.0	2.5	3	3
I/I_o =	23	24	24	24	24 ($\Delta r = \Delta z = a/2$)

The last column indicates that halving Δr and Δz did not change the result noticeably.

The above results suggest that the use of a finite z-boundary results in an underestimate of the current. When the boundary is artifically placed too near, the resulting potential falls off too rapidly near the probe, causing a reduction (due to the increased field strength) in the number of trajectories which escape to infinity.

One further numerical result which is consistent is the insensitivity of the attracted-particle density at a point near the probe to changes in the potential near the boundary. Consider, for example, the 3 potential distributions given by Table F-3.

TABLE F-3

Test Potential Distributions

	A				B				C			
z/a	r=0	a	2a	3a	r=0	a	2a	3a	r=0	a	2a	3a
3.0	- .66	- .66	-.61	-.56	- .33	- .33	-.31	-.28	- .97	- .82	-.40	-.25
2.5	- .97	- .82	-.40	-.25	- .97	- .82	-.40	-.25	- .97	- .82	-.40	-.25
2.0	-1.3	-1.1	-.38	-.25	-1.3	-1.1	-.38	-.25	-1.3	-1.1	-.38	-.25
1.5	-3.1	-2.5	-.52	-.29	-3.1	-2.5	-.52	-.29	-3.1	-2.5	-.52	-.29
1.0	-7.1	-5.5	-.72	-.31	-7.1	-5.5	-.72	-.31	-7.1	-5.5	-.72	-.31
0.5	-15	(-11)	-.73	-.31	-15	(-11)	-.73	-.31	-15	(-11)	-.73	-.31
0	-45.54	-22.77	0	0	-45.54	-22.77	0	0	-45.54	-22.77	0	0

The three distributions (A, B, C) are identical in all but the outermost row at z = 3a, which is halved in B, and is the duplicate of the next row in C. The density is calculated at the position marked by parentheses, and has the values 0.59, 0.57, and 0.59, respectively, for Distributions A, B, and C.

TABLE 1

Laplace Potential Distribution. Mach Zero(a-c)

Axial Position	Radial Position r/a						
z/a	0.0	0.5	1.0	1.5	2.0	2.5	3.0
3.00	2.34	2.26	2.04	1.75	1.44	1.15	0.903
2.75	2.74	2.64	2.35	1.97	1.58	1.23	0.943
2.50	3.26	3.11	2.73	2.22	1.73	1.30	0.977
2.25	3.92	3.72	3.19	2.52	1.89	1.38	1.00
2.00	4.81	4.51	3.77	2.86	2.05	1.44	1.01
1.75	6.00	5.57	4.49	3.24	2.20	1.48	1.00
1.50	7.65	7.00	5.41	3.67	2.33	1.48	0.967
1.25	9.98	9.00	6.60	4.10	2.40	1.43	0.899
1.00	13.3	11.9	8.14	4.49	2.36	1.32	0.793
0.75	18.2	16.1	10.1	4.67	2.15	1.11	0.645
0.50	25.2	22.5	12.8	4.33	1.68	0.817	0.457
0.25	34.5	32.2	16.5	2.87	0.943	0.434	0.238
0.00	45.54	45.54	22.77	0.0	0.0	0.0	0.0

(a) Potential energy in units of kT = 0.112 volts. All values are positive for electrons, but become negative for ions.

(b) Probe potential = -5.1 volts at 1300°K

(c) Probe radius a = 3.33 cm, Debye length infinite

TABLE 2

Laplace Ion Current versus Probe Potential. Mach Zero[(a-b)]

Volts	ϕ	I/I_o
1.12	10.	.000
.560	5.	.004
.224	2.	.132
.112	1.	.359
.056	.5	.603
.022	.2	.814
.011	.1	.899
0.	0.	1.00
- .011	- .1	1.09
- .022	- .2	1.18
- .056	- .5	1.44
- .112	- 1.	1.86
- .224	- 2.	2.66
- .560	- 5.	5.01
- 1.	- 8.93	8.05
- 2.	-17.9	14.8
- 3.	-26.8	21.4
- 4.	-35.7	28.0
- 5.	-44.6	34.3
- 5.1	-45.5	35.3
- 6.	-53.6	40.8
- 7.	-62.5	47.1
- 8.	-71.4	53.4
- 9.	-80.4	59.7
-10.	-89.3	65.6

(a) kT = 0.112 volts, s = 0.2 cm.

(b) Collecting radius = 1.665 cm.

TABLE 3

Laplace Attracted-Ion Current versus Ion Mach Number$^{(a-c)}$

M	I/I_o	j_1/j_0	j_2/j_0	j_3/j_0	% Spread
0	34.8				
.5	24.5	24.7	25.4	23.6	7
1.0	15.6	15.5	15.7	15.5	1
1.5	9.5	9.4	9.2	9.8	6
2.0	6.0	6.1	5.6	6.4	13
3.0	3.2	3.5	2.8	3.5	22
4.0	2.2				
6.0	1.4				

(a) kT = 0.112 volts, s = 0.025 cm.

(b) Probe potential = -5.1 volts.

(c) Collecting radius = 1.665 cm.

TABLE 4

Poisson Potential Distribution. Mach Zero(a-c)

Axial Position z/a	Radial Position r/a						
	0.0	0.5	1.0	1.5	2.0	2.5	3.0
3.00	0.475	0.458	0.404	0.340	0.277	0.215	0.170
2.75	0.542	0.513	0.432	0.363	0.297	0.219	0.176
2.50	0.799	0.755	0.621	0.483	0.367	0.223	0.178
2.25	1.32	1.23	0.972	0.678	0.430	0.228	0.179
2.00	2.08	1.92	1.44	0.903	0.503	0.238	0.180
1.75	3.20	2.92	2.08	1.19	0.566	0.247	0.179
1.50	4.80	4.35	2.99	1.57	0.665	0.252	0.174
1.25	7.17	6.44	4.25	2.03	0.782	0.250	0.164
1.00	10.7	9.50	5.99	2.55	0.878	0.244	0.150
0.75	15.9	14.0	8.41	3.04	0.917	0.224	0.129
0.50	23.6	20.6	11.7	3.24	0.826	0.178	0.097
0.25	35.2	30.5	16.3	2.61	0.527	0.106	0.058
0.00	45.54	45.54	22.77	0.0	0.0	0.0	0.0

(a) Potential energy in units of kT = 0.112 volts. All values are positive for electrons, but become negative for ions.

(b) Probe potential = -5.1 volts at 1300°K.

(c) Probe radius a = 3.33 cm, Debye length = 1.0 cm.

TABLE 5

Poisson Potential Distribution. Ion Mach 3(a-c)

Axial Position z/a	Radial Position r/a						
	0.0	0.5	1.0	1.5	2.0	2.5	3.0
1.50	4.2	3.7	2.4	1.4	.87	.58	.38
1.25	5.5	4.9	2.9	1.4	.62	.39	.34
1.00	8.6	7.5	4.3	1.6	.51	.28	.26
0.75	14	12	6.7	2.0	.44	.18	.19
0.50	22	19	10	2.3	.33	.066	.12
0.25	34	29	15	2.0	.17	-.039(d)	.023
0.00	46	46	23	0.0	0.0	0.0	0.0

(a) Potential energy in units of kT = 0.112 volts. All values are positive for electrons, but become negative for ions.

(b) Probe potential = 5.1 volts.

(c) Probe radius a = 3.33 cm, Debye length = 1.0 cm.

(d) Potential has change in sign at this point.

TABLE 6

Attracted-Ion Current Density versus Radius[(a-c)]

Mach Zero	I/I_o	(r=0) j/j_o	(r=0.19) j_1/j_o	(r=0.83) j_2/j_o	(r=1.48) j_3/j_o
Laplace ($\lambda_D = \infty$)	35.7	35.5	35.1	36.6	34.8
Poisson (λ_D = 1 cm)	24.9	33.3	33.5	28.6	20.5
Ion Mach 3					
Laplace ($\lambda_D = \infty$)	3.2	--	3.5	2.8	3.5
Poisson (λ_D = 1 cm)	2.4	--	2.7	2.1	2.7

(a) kT = 0.112 volts, s = 0.025 cm.

(b) Probe potential = -5.1 volts.

(c) Collecting radius = 1.665 cm.

TABLE 7

Attracted-Ion Density Distribution. Mach Zero[(a-d)]

Axial Position z/a	Radial Position r/a 0.0	0.5	1.0	1.5	2.0	2.5	3.0
3.00	-	-	-	-	-	-	-
2.75	-	.65 (1.6)	.63 (1.6)	.49 (.8)	.51 (3.2)	.49 (3.2)	-
2.50	-	.51 (.8)	.51 (.2)	.50 (.8)	.47 (3.2)	.51 (3.2)	-
2.25	-	.37 (.4)	.38 (.4)	.41 (.8)	.48 (3.2)	.52 (3.2)	-
2.00	-	.37 (.2)	.38 (.2)	.40 (.8)	.45 (3.2)	.50 (1.6)	-
1.75	-	.31 (.2)	.35 (.2)	.41 (.4)	.45 (.4)	.46 (.8)	-
1.50	-	.33 (.1)	.34 (.2)	.39 (.4)	.44 (.4)	.44 (.4)	-
1.25	-	.35 (.1)	.34 (.2)	.34 (.4)	.40 (.4)	.43 (.4)	-
1.00	-	.38 (.05)	.37 (.05)	.36 (.2)	.39 (.2)	.40 (.4)	-
0.75	-	.38 (.05)	.37 (.05)	.36 (.2)	.36 (.2)	.38 (.4)	-
0.50	-	.45 (.05)	.36 (.05)	.32 (.2)	.34 (.2)	.38 (.2)	-
0.25	-	.55 (.025)	.49 (.025)	.40 (.05)	.29 (.8)	.34 (.8)	-
0.00	-	-	-	-	-	-	-

(a) Density in units of normal density at infinity.

(b) Probe potential = -5.1 volts at 1300°K.

(c) Probe radius a = 3.33 cm, Debye length ≐ 1.0 cm.

(d) Numbers in parentheses are trajectory step sizes.

TABLE 8

Repelled-Electron Density Distribution. Mach Zero[(a-c)]

Axial Position z/a	Radial Position r/a 0.0	0.5	1.0	1.5	2.0	2.5	3.0
3.00	-	-	-	-	-	-	-
2.75	-	.37	.36	.34	.45	.48	-
2.50	-	.20	.26	.37	.50	.45	-
2.25	-	.18	.27	.37	.45	.45	-
2.00	-	.15	.23	.32	.45	.43	-
1.75	-	.076	.15	.27	.34	.43	-
1.50	-	.027	.087	.22	.34	.42	-
1.25	-	.0076	.038	.16	.31	.41	-
1.00	-	.0002	.012	.098	.26	.41	-
0.75	-	0	.0011	.056	.22	.40	-
0.50	-	0	0	.026	.20	.39	-
0.25	-	0	0	.018	.16	.37	-
0.00	-	-	-	-	-	-	-

(a) Density in units of normal density at infinity.

(b) Probe potential = -5.1 volts at 1300°K.

(c) Probe radius a = 3.33 cm, Debye length = 1.0 cm.

TABLE 9

Attracted-Ion Density Distribution. Ion Mach 3(a-d)

Axial Position	Radial Position r/a						
z/a	0.0	0.5	1.0	1.5	2.0	2.5	3.0
1.50	-	-	-	-	-	-	-
1.25	-	1.1 (.2)	1.1 (.2)	1.0 (.8)	.98 (.8)	.95 (1.6)	-
1.00	-	1.1 (.2)	.99 (.2)	.98 (.8)	.95 (.8)	.97 (1.6)	-
0.75	-	1.1 (.025)	.96 (.05)	.92 (.2)	.92 (.8)	.96 (.8)	-
0.50	-	1.1 (.025)	.96 (.025)	.85 (.05)	.90 (.8)	.97 (.8)	-
0.25	-	1.1 (.025)	1.0 (.0125)	.87 (.0125)	.83 (.4)	1.0 (.8)	-
0.00	-	-	-	-	-	-	-

(a) Density in units of normal density at infinity.

(b) Probe potential = -5.1 volts at 1300°K.

(c) Probe radius a = 3.33 cm, Debye length = 1.0 cm.

(d) Numbers in parentheses are trajectory step sizes.

TABLE 10

Repelled-Electron Density Distribution. Ion Mach 3[(a-c)]

Axial Position z/a	Radial Position r/a 0.0	0.5	1.0	1.5	2.0	2.5	3.0
1.50	-	-	-	-	-	-	-
1.25	-	.0050	.046	.13	.17	.26	-
1.00	-	0	.0086	.13	.24	.28	-
0.75	-	0	.0001	.069	.26	.29	-
0.50	-	0	0	.043	.23	.34	-
0.25	-	0	0	.033	.22	.40	-
0.00	-	-	-	-	-	-	-

(a) Density in units of normal density at infinity.

(b) Probe potential = -5.1 volts at 1300°K.

(c) Probe radius a = 3.33 cm, Debye length = 1.0 cm.

TABLE 11

Velocity Distribution (dj/dZ) versus Radius. Poisson Mach Zero(a-d)

	(Step)		(r=0)	(r=0.19)	(r=0.83)	(r=1.48)
Z	S	dI/dZ	dj/dZ	dj_1/dZ	dj_2/dZ	dj_3/dZ
40.00	.05		.880			
	.025		1.000			
	.0125		1.000			
45.50	.05	.783	1.000	.995	.837	.708
45.54	.05	.775	1.000	.982	.830	.700
	.025	.858	1.000	1.000	.932	.774
	.0125	.915	1.000	1.000	.999	.828
45.60	.05	.766	.9418(e)	.9418(e)	.818	.697
	.025	.845		.9418(e)	.926	.759
	.0125	.883		.9418(e)	.9418(e)	.822
46.00	.05	.628		.6313(f)	.6313(f)	.624

(a) kT = 0.112 volts.

(b) Probe potential = −5.1 volts, $\phi = -45.54$.

(c) Collecting radius = 1.665 cm.

(d) I and j in multiples of I_o and j_o, respectively.

(e) 0.9418 = exp(−0.06).

(f) 0.6313 = exp(−0.46).

TABLE 12

Ion Central Current. Isolated Satellite in Laplace Field(a-d)

	M = 0(e)		M = 1	M = 1	M = 1	M = 1.414
ϕ			$\gamma = 0°$	$\gamma = 45°$	$\gamma = 90°$	$\gamma = 45°$
0	0.999		3.54	2.65	0.980	3.62
- 5	5.07	(5.07)	9.73	8.03	3.93	8.47
-10	8.92	(8.94)	16.7	13.7	6.38	13.6
-15	12.7	(12.8)	24.5	19.7	8.50	19.2
-20	15.8	(16.6)	32.5	25.4	10.2	24.7
-25	19.3	(20.3)	41.3	31.4	12.0	30.3
-30	22.9	(24.1)	50.5	37.5	13.6	36.2
-35	26.5	(27.9)	60.7	44.0	15.0	42.4
-40	30.0	(31.7)	70.5	50.2	16.6	48.4
-45	33.6	(35.4)	81.2	56.5	17.9	54.5
-50	37.1	(39.1)	92.1	62.8	19.3	60.6

(a) Probe potential = ϕkT, where kT = 0.112 volts.

(b) M = Mach number, γ = Mach angle with respect to probe normal.

(c) Step size = 0.05 cm.

(d) Satellite height and radius 100 cm and 50 cm, respectively. Probe radius 3.33 cm.

(e) Numbers in parentheses are more accurate (see text).

TABLE 13

Photoelectron Central Current. Isolated Satellite in Laplace Field(a-c)

E_o (volts)	$(1 - \phi)$	$\gamma_s = 0°$	$\gamma_s = 35°$	$\gamma_s = 45°$	$\gamma_s = 90°$
0.1	151	26.1	21.4	18.4	0
1.0	16	2.16	1.77	1.52	0
5.0	4	0.222	0.182	0.157	0

$E_o = 0.1$ volt

$(\sin\alpha_c = 0.864)$

$\sin\alpha$	x_s (cm)
0.867	-10.8
0.879	4.03
0.898	4.06
0.922	3.85
0.947	3.43
--	< 3.33

$E_o = 1.0$ volt

$(\sin\alpha_c = 0.896)$

$\sin\alpha$	x_s (cm)
0.898	4.62
0.907	4.32
0.921	4.05
0.940	3.79
0.959	3.35
--	< 3.33

$E_o = 5.0$ volt

$(\sin\alpha_c = 0.943)$

$\sin\alpha$	x_s (cm)
0.944	5.48
0.949	4.79
0.957	4.22
0.967	3.75
--	< 3.33

(a) Current density in multiples of emitted photocurrent density for normal solar incidence.

(b) Probe potential 15 volts.

(c) Satellite height and radius 100 cm and 50 cm, respectively. Probe radius 3.33 cm.

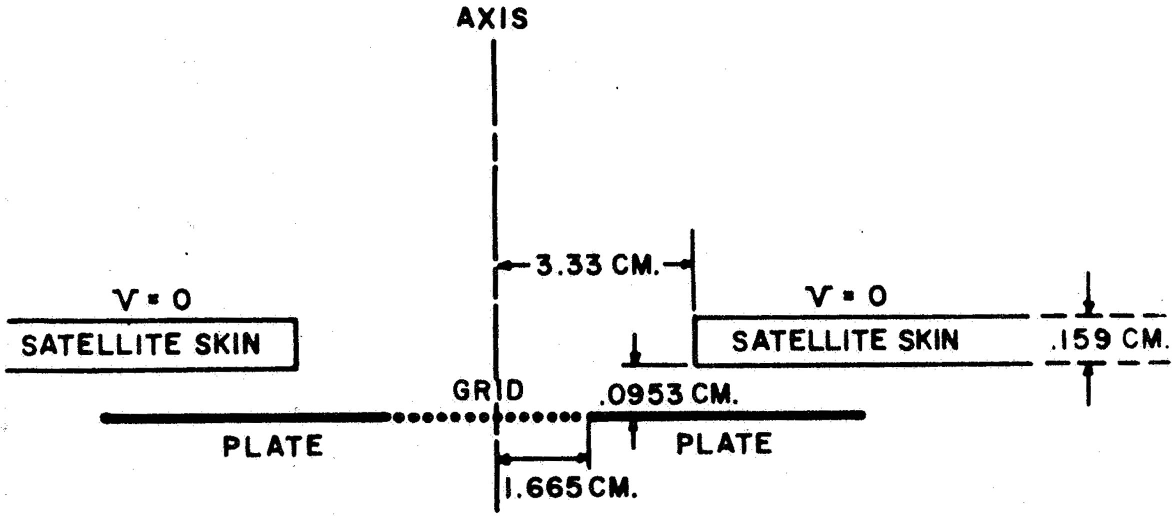

FIGURE 1. OGO PLANAR PROBE GEOMETRY

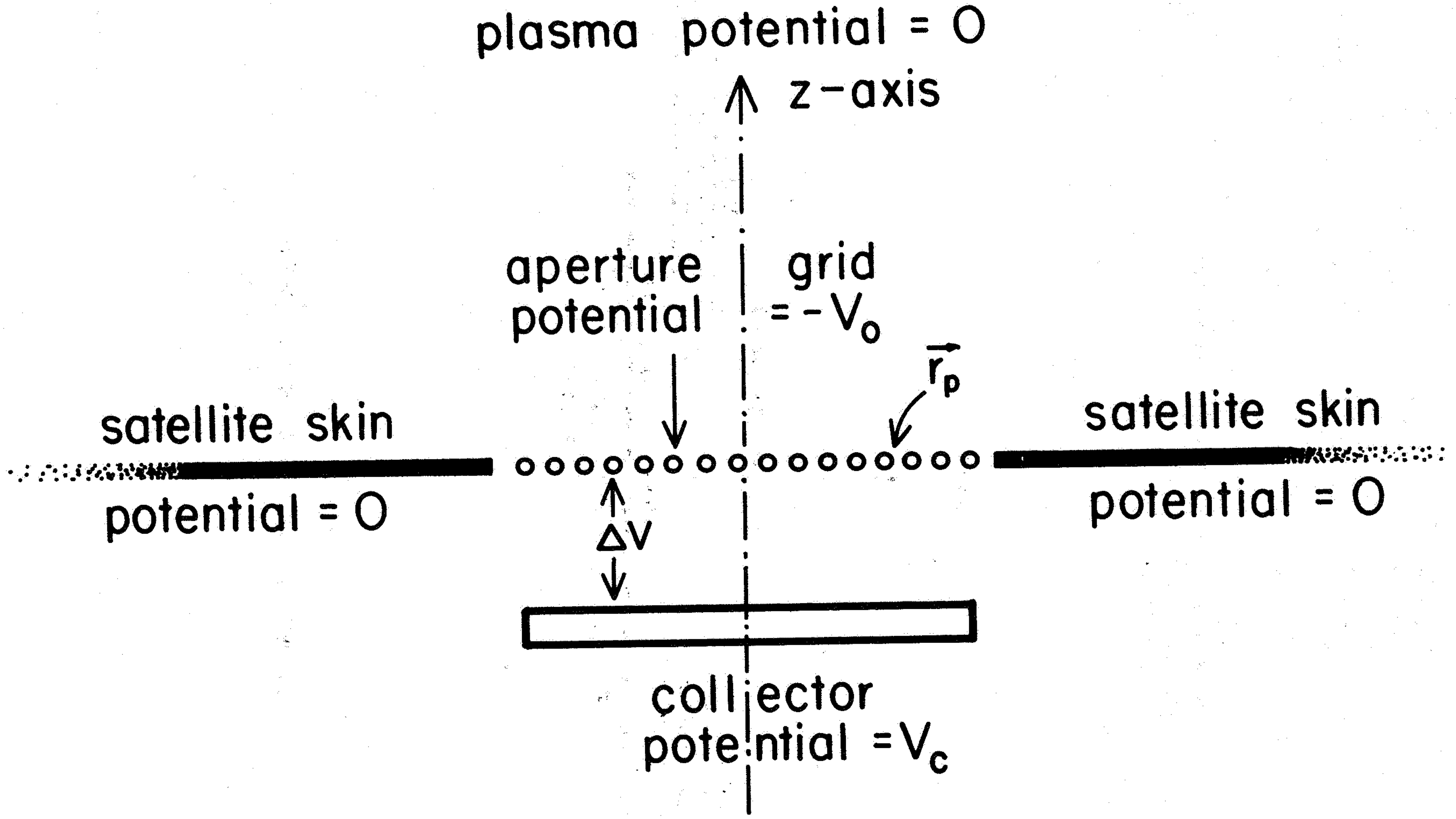

FIGURE 2. IDEALIZED GEOMETRY WITH COLLECTOR

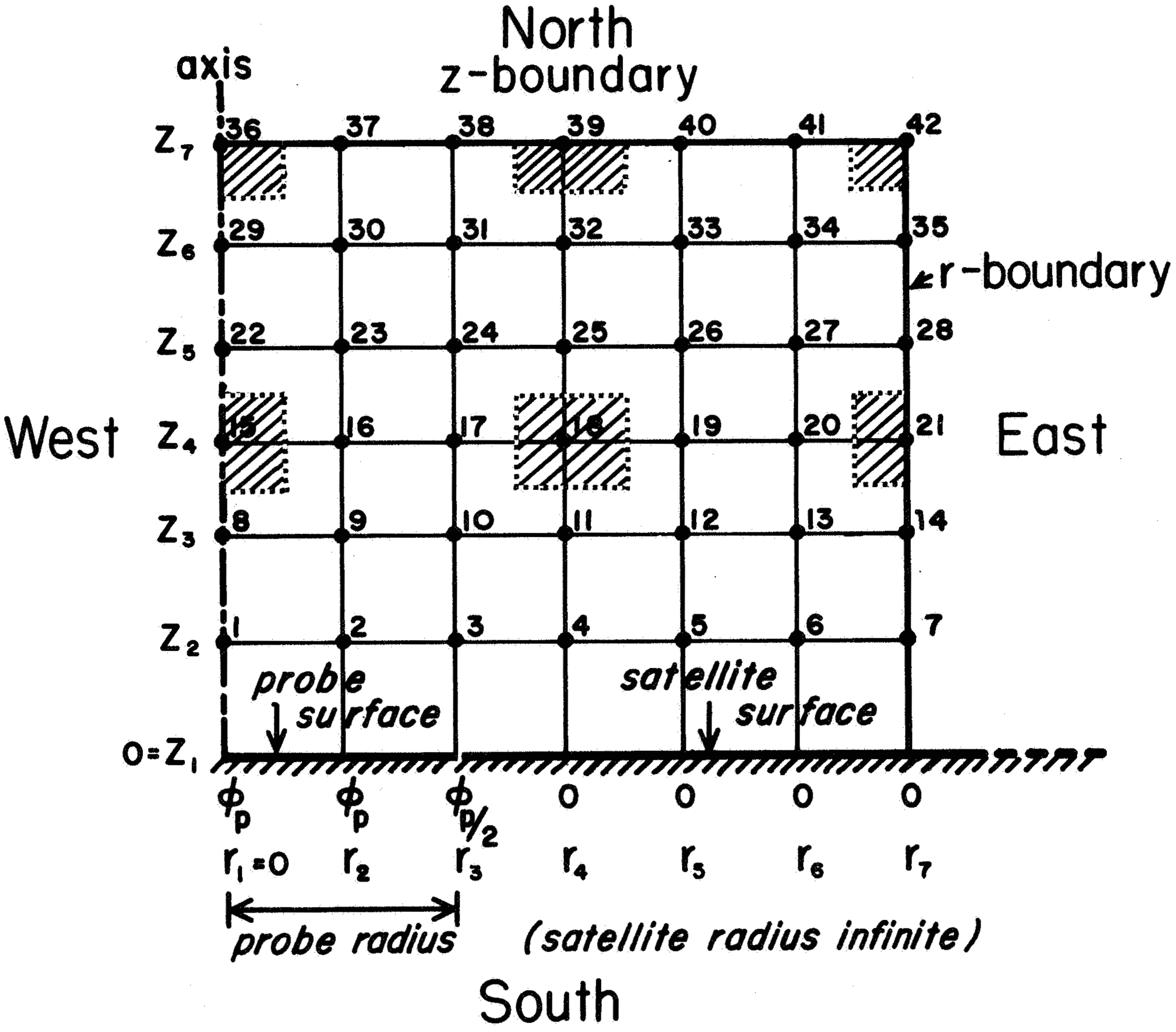

FIGURE A-1. DIFFERENCE EQUATION GRID FOR INFINITE SATELLITE

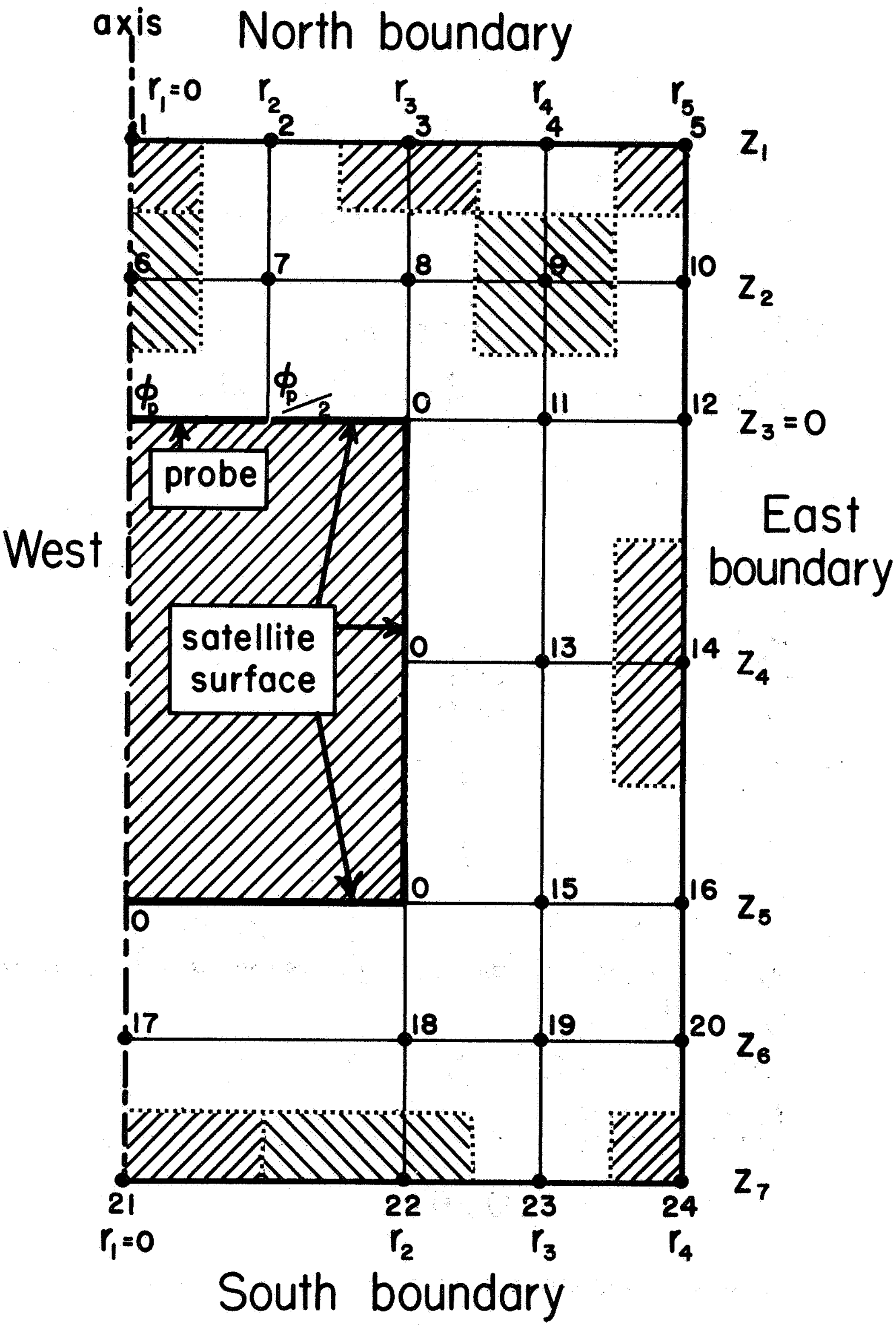

FIGURE A-2. DIFFERENCE EQUATION GRID FOR ISOLATED SATELLITE

REFERENCES

1. L. W. Parker, "A computer program for calculating the charge distribution about a space vehicle," NASA CR-401, March 1966. Presented to the American Astronautical Society Second Symposium on Interaction of Space Vehicles with an Ionized Atmosphere, Miami Beach, 26-27 November 1965.

2. L. W. Parker and E. C. Whipple, Jr., "Theory of a satellite electrostatic probe," Annals of Physics 44(1), 126-161 (1967).

3. The geometry in Fig. 1 was designed by E. C. Whipple, Jr. for the OGO satellite.

4. G. Medicus (private communication).

5. J. G. Laframboise, "Theory of spherical and cylindrical Langmuir probes in a collisionless Maxwellian plasma at rest," University of Toronto Institute for Aerospace Studies Report No. 100, June 1966.